The effect of stable thermal stratification on turbulent boundary layer statistics

O.Williams, T. Hohman, T. Van Buren, E. Bou-Zeid and A. J. Smits

May 22, 2019

Abstract

The effects of stable thermal stratification on turbulent boundary layers are experimentally investigated for smooth and rough walls. Turbulent stresses for weak to moderate stability are seen to scale with the wall-shear stress compensated for changes in fluid density in the same manner as done for compressible flows, suggesting little change in turbulent structure within this regime. At higher levels of stratification turbulence no longer scales with the wall shear stress and turbulent production by mean shear collapses, but without the preferential damping of near-wall motions observed in previous studies. We suggest that the weakly stable and strongly stable (collapsed) regimes are delineated by the point where the turbulence no longer scales with the local wall shear stress, a significant departure from previous definitions. The critical stratification separating these two regimes closely follows the linear stability analysis of Schlichting (1935) [Schlichting, *Hauptaufsätze. Turbulenz bei Wärmeschichtung*, ZAMM-J. of App. Math. and Mech., vol 15, 1935] for both smooth and rough surfaces, indicating that a good predictor of critical stratification is the gradient Richardson number evaluated at the wall. Wall-normal and shear stresses follow atmospheric trends in the local gradient Richardson number scaling of Sorbjan (2010) [Sorbjan, *Gradient-based scales and similarity laws in the stable boundary layer*, Q.J.R. Meteorological Soc., vol 136, 2010], suggesting that much can be learned about stratified atmospheric flows from the study of laboratory scale boundary layers at relatively low Reynolds numbers.

1   Introduction

The atmospheric surface layer is often stably stratified. For example, the nocturnal boundary layer at moderate latitudes can experience significant radiative cooling of the surface, resulting in a stable stratification. Stability can also occur when warm air masses flow (by advection or subsidence) over cold seas or ice, as in polar regions. Our understanding of these flows remains incomplete, and the current models are often insufficient to fully describe their behavior (Mahrt, 1998, 2014). Atmospheric measurements within the thermally stable regime are generally difficult since flow unsteadiness increases and flux magnitudes decrease with increasing stability, leading to larger relative errors. Reductions in the integral scale also make turbulence-resolving simulations

1

more challenging (Bou-Zeid *et al.*, 2010), further reducing the number of tools available for probing the dynamics of stable flows. Laboratory experiments can therefore play an important role. While the Reynolds numbers are typically low compared to the atmosphere, the boundary conditions can be tightly controlled and other influences such as diurnal variations can be excluded. We present extensive laboratory measurements of thermally stratified boundary layers over smooth and rough isothermal walls, and make detailed comparisons with atmospheric data.

The degree of stratification is usually described in terms of a Richardson number. The ratio of the buoyancy flux and turbulent production by mean shear in the turbulent kinetic energy (TKE) equation is called the flux Richardson number,

$$Ri_f = \frac{g}{T_0} \frac{\overline{w\theta}}{\overline{uw}\,(\partial U/\partial z)}, \tag{1}$$

where $\overline{w\theta}$ is the wall-normal heat flux and $\overline{uw}$ is the Reynolds shear stress. Here, z is the wall-normal direction, g is the acceleration due to gravity, and T_0 is a reference temperature, here chosen to be the freestream temperature. Temperature fluctuations are denoted by the variable θ, and velocity fluctuations are indicated by u, v and w, relative to the mean velocities U, V and W in the x- (streamwise), y- (spanwise), and z- (wall-normal) directions, respectively. The overline denotes an ensemble average.

More easily measured, and related to the flux Richardson number through the turbulent Prandtl number Pr_t, is the gradient Richardson number, defined in terms of the mean gradients of temperature and streamwise velocity so that

$$Ri = \frac{g}{T_0} \frac{\partial T/\partial z}{(\partial U/\partial z)^2} = \frac{N^2}{(\partial U/\partial z)^2} = Pr_t\, Ri_f. \tag{2}$$

Here, $N = \sqrt{(g/T_0)\partial T/\partial z}$ is the Brunt-Väisälä frequency (a measure of static stability). The turbulent Prandtl number has conventionally been assumed to be close to unity for neutrally and weakly stratified layers, but it can increase significantly at higher stratification levels (see Katul *et al.* (2014); Zilitinkevich *et al.* (2013)).

In experimental studies, the bulk Richardson number Ri_δ is often used and defined as

$$Ri_\delta = \frac{g\delta}{T_0} \frac{\Delta T}{U_\infty^2}. \tag{3}$$

Here, ΔT is the temperature difference across a boundary layer of thickness δ. For stable stratification, all Richardson numbers are positive.

A number of laboratory experiments have been performed to complement the studies in the atmosphere (Nicholl, 1970; Arya & Plate, 1969; Plate & Arya, 1969; Arya, 1975; Piat & Hopfinger, 1981; Ogawa *et al.*, 1982, 1985; Ohya *et al.*, 1997; Ohya, 2001; Ohya & Uchida, 2003, 2004; Puhales *et al.*, 2015; Demarco *et al.*, 2015). Of these, the studies by Arya ($Ri_\delta < 0.1$), Ogawa *et al.* ($Ri_\delta < 0.25$), Ohya *et al.* ($Ri_\delta < 1.33$), Ohya ($Ri_\delta < 1.31$) and Demarco *et al.* ($Ri_\delta < 0.06$) allowed the thermal boundary layer to develop over a heated or cooled wall without prescribing a particular temperature profile. Based on this work, it is now well-known that turbulence is rapidly suppressed by increasing stratification as energy is extracted from the $\overline{w^2}$ (direct buoyant destruction)

2

and $-\overline{uw}$ (suppression of shear generation) stresses due the additional energy required to overcome buoyancy.

In an important observation, Ohya *et al.* (1997) identified the transition between a weakly stable regime and a strongly stable regime (on a smooth wall) as the point where the peak in the turbulent stresses moved far into the outer layer and near-wall turbulence was strongly damped, creating a region of small counter-gradient heat flux. Internal gravity waves and Kelvin-Helmholtz instabilities were also observed at high stratification levels. In Ohya *et al.* (1997), and a later rough-wall experiment (Ohya, 2001), the two regimes were delineated by a critical bulk Richardson number, $Ri_{\delta,cr}$ = 0.25, which Ohya interpreted as being an expected value since it agreed with the classical result of Taylor (1931) and Miles & Howard (1964) for the instability of a laminar flow with constant shear.

In this respect, Schlichting (1935, 1979) conducted a more complete analysis of the instability of laminar shear flows that accounted for profile curvature, which is necessary to characterize the critical layer and global stability of the boundary layer. His stability curves were expressed in terms of the gradient Richardson number evaluated at the wall, and the results were Reynolds-number and weakly Froude-number dependent. A high Reynolds number asymptote of $Ri_{w,cr}$ = 1/24 (= 0.042) was demonstrated for Fr = 0. Schlichting's analysis does not seem to have been widely appreciated, and no detailed comparison with experimental data appears to have been performed until now.

The interpretation of Ohya *et al.*'s results is further complicated by the fact that their levels of freestream turbulence increased (as a fraction of the freestream velocity) with increasing Richardson number, since the Richardson number was increased by reducing the freestream velocity. As a result, the outer layer turbulence peak they observed in the streamwise and wall-normal directions for strong stratification is comparable in magnitude to their freestream turbulence level of 3-4% of U_∞.

The applicability of laboratory results to our understanding of the atmospheric surface layer is also an open question. In laboratory scale experiments with significant stratification, that is, high Richardson number, the Reynolds number is usually small, simply because the Richardson number is proportional to U_∞^{-2} and the boundary layer thickness, δ. To date, this problem has only been examined by Plate & Arya (1969) who demonstrated a correspondence between Monin-Obukhov Similarity Theory (MOST) and the experiments of Arya (1968) over a limited range of wall-normal positions ($0.01 \leq z/\delta \leq 0.15$). This dataset was expanded by Arya (1975). The functional forms (logarithmic or power law) and their coefficients, however, were found to be significantly different than those subsequently established for the atmospheric surface layer (Stull, 1988), suggesting that Reynolds number effects are important. The influence of the Reynolds number was also corroborated by numerical studies and theoretical analyses of Chung & Matheou (2012) and Shah & Bou-Zeid (2014). To complicate matters further, the Reynolds and Richardson numbers vary simultaneously with increasing stability, so that it is difficult to discriminate between the effects of buoyancy and inertia. Somewhat surprisingly, previous laboratory work has only examined changes in turbulence intensity relative to the freestream velocity. Such a scaling does not remove Reynolds number effects in neutrally stable flows, and therefore it is unlikely to isolate the effects due to stratification alone.

Here, we use particle image velocimetry (PIV) and thermocouple rakes to examine a wide range of low-Reynolds number, thermally stratified boundary layers with bulk stratifications as strong as $Ri_\delta \approx 0.25$. Experiments were conducted for both smooth and rough walls to improve correspondence with the atmospheric surface layer, where the wall is almost always fully rough. Coriolis forces were not considered. Despite the Ekman turning of the mean flow induced by Coriolis forces, such forces have been shown to cause little effect on turbulent statistics for weak to moderate stability in atmospheric measurements (Grachev *et al.*, 2005), and although they grow in influence as the fluxes reduce for stronger levels of stability, it then becomes difficult to discriminate between stratification and Coriolis effects. As such, the absence of this force in the current experiments can be considered an asset.

In an effort to isolate the effects of Reynolds number, we use inner and outer similarity variables commonly used when scaling wall-bounded turbulent flows. For the inner and outer regions of the layer the velocity scale is the friction velocity $u_\tau = \sqrt{\tau_w/\rho_w}$, where τ_w is the wall stress, and ρ_w is the fluid density at the wall. For the inner part, the length scale is ν_w/u_τ, where ν_w is the kinematic viscosity at the wall, and for the outer part the length scale is δ. We find good correspondence over much of the boundary layer between our low Reynolds number laboratory experiments and atmospheric data in the gradient-based atmospheric scaling of Sorbjan (2010), which suggests that our results are broadly applicable across all Reynolds numbers. In particular, we propose that the weak/strong criterion suggested by Ohya *et al.* (1997) needs to be modified.

2 Experimental Setup

The experiments were conducted in Princeton Gas Dynamics Laboratory's low-speed wind tunnel. The tunnel is open-return and is 5 m long with a 1.2×0.9 m^2 cross-section and a maximum freestream velocity of $U_\infty = 2.4$ m/s. In previous laboratory studies of stratified boundary layers, heated air was passed over a cooled bottom surface. In our experiment, air enters the tunnel at room temperature before passing under a strongly heated upper surface, as shown in figure 1, creating a stable buoyancy force that acts upwards toward the surface. The upper surface is made up of a 12.7-mm-thick sheet of aluminum that can be isothermally heated along its entire length to a maximum temperature of $135 \pm 2°C$ using a set of 32 resistive heating strips. A nominally zero pressure gradient turbulent boundary layer develops over the upper surface, tripped using a 6.35 mm (1/4") rod located at the leading edge of the heated plate. The measurement region was located a distance of 3.75 m downstream of the trip.

Note that for a heated surface, the density and viscosity decrease with distance from the wall, whereas with a cooled surface the trend is reversed. The high wall-temperatures employed in our study cause the density and viscosity to vary by up to 30% from the wall to freestream, so that the kinematic viscosity can be up to 80% larger at the wall than that in the freestream. These fluid property variations need to be taken into account, particularly when assessing Reynolds number effects, as we will show. Dilatation effects may also be important, and it will be examined how such effects can be accounted for in the scaling.
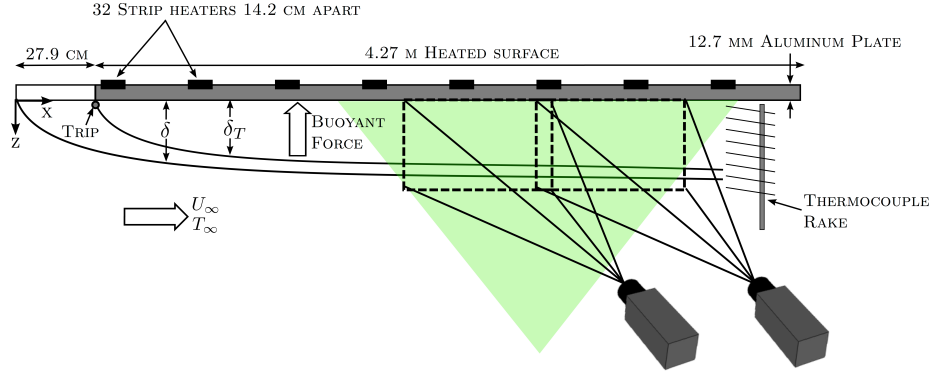
4

Figure 1: A schematic of the experimental setup.

Tests were conducted using both smooth and rough surfaces. For the rough surface, a woven wire mesh of thickness k = 4.1 mm was used, similar to that studied by Flack *et al.* (2005) and Flack *et al.* (2007). The wire mesh was a square weave with a wire size of 2.05 mm and a pitch of 12.7 mm, oriented with the wires running in the streamwise and spanwise directions. All PIV data were acquired in a streamwise-vertical plane located between two streamwise wires. For the neutrally stratified cases, the roughness height corresponds to δ/k = 30-31 and k^+ = 11-39, where the superscript + denotes normalization using the friction velocity scale u_τ and the inner length scale ν_w/u_τ.

Roughness causes a downward shift in the logarithmic portion of the mean velocity profile by an amount called the roughness function, ΔU^+. Nikuradse (1933) proposed that different roughness geometries could be compared by defining a roughness length scale k_s, called the equivalent sandgrain roughness, defined in terms of the roughness function so that

$$\Delta U^+ = \frac{1}{\kappa} ln\left(k_s^+\right) + B - 8.5. \tag{4}$$

We found k_s^+ = 44-124 for the neutrally stratified boundary layer cases reported here. In eqn. 4, κ and B are, respectively, the von Kármán constant and the additive constant in the logarithmic law for the mean velocity profile. The values were taken to be κ = 0.421 and B = 5.6 (McKeon *et al.*, 2004), but our conclusions are not sensitive to the choice of log-law constants. Note that the roughness length z_0, scaled using inner variables, is given by $z_0^+ = \exp\left[\kappa(\Delta U^+ - B)\right]$.

The values of δ/k and k^+ are close to those found in other studies using woven wire mesh where outer similarity was observed (Connelly *et al.*, 2006; Flack *et al.*, 2007), indicating that the effects of roughness are confined to a roughness sublayer near the wall in line with Townsend's wall-similarity hypothesis (Townsend, 1976). Such flows are termed fully-rough (Jimenez, 2004).

Large field-of-view, two dimensional, two-component velocity measurements were obtained in the (*x*-*z*)-plane using PIV. The large field-of-view was created by partially overlapping two 5.5 megapixel sCMOS camera images in the streamwise direction

5

(see figure 1). The resulting vector fields could then be merged into a 160×300 mm^2 domain, which corresponded to approximately $1.25\delta \times 2.3\delta$ for neutral conditions.

Light was provided by a 50 mJ dual-pulse Nd:YAG laser in conjunction with a Powell lens to create the light sheet and a focal lens to narrow the sheet thickness in the measurement domain (~ 1 mm). The flow was seeded using 1 μm mineral oil smoke particles generated by a MAX 3000 MDG fog generator.

The velocities were computed using a multi-grid, multi-pass cross-correlation method with iterative image deformation (Huang *et al.*, 1993; Jambunathan *et al.*, 1995; Nogueira *et al.*, 1999; Scarano, 2002) as implemented in DaVis 8.1.6. The two camera frames were merged using functions internal to DaVis. The window size of the final pass was 32×32 pixels with a 50% overlap, resulting in a grid spacing of $\Delta x^+ = \Delta z^+$ = 3-12 for the neutrally stratified smooth and rough wall cases. The friction velocity was found to decrease substantially with stable thermal stratification, improving the grid spacing to values as low as $\Delta x^+ = \Delta z^+$ = 1.5.

Due to drop-outs in near-wall seeding at the highest wall temperatures, special care was taken to remove spurious vectors. This was initially accomplished by removing all vectors with a peak ratio of less than 1.1, in conjunction with a normalized median filter (Westerweel & Scarano, 2005) greater than two standard deviations of a 5×5 neighborhood. No filtered vectors or alternate correlation peaks were reinserted at this stage. Under neutral conditions the valid-vector yield was 99%. With increasing wall temperature, an increasing number of near-wall vectors were determined to be invalid, and so we mark the wall distance below which at least 10% of vectors were missing as $z_{10\%}$.

A small number of vectors were reinserted from alternate correlation peaks, satisfying a normalized local median filter of three standard deviations. This had the effect of filling a small number of data holes while having a negligible impact on vector statistics above $z_{10\%}$. It also had the effect of slightly increasing data yield towards the wall, but since these vectors were derived from small peak ratios, any data presented below $z_{10\%}$ is shown using dotted lines.

Finally, a narrow-band Gaussian spatial filter was employed to remove noise associated with frequencies larger than the sampling frequency of the interrogation, as is now common practice (Adrian *et al.*, 2000; Wu & Christensen, 2006). For all flow speeds and wall temperatures, 700 image pairs were acquired at a rate of 15 Hz.

Bias errors due to peak locking were limited by ensuring particle image sizes were greater than two pixels. Under these conditions the random error was dominated by noise in particle image recording, which accounted for approximately 5% of the particle image diameter or approximately 0.1 pixels, as shown by Prasad *et al.* (1992). Interframe times were selected to maintain a freestream particle displacement of approximately 8 pixels and thus random errors in velocity were estimated to be approximately 1.25% of the freestream velocity. Other errors due to convergence of statistics and merging of velocity fields yielded total uncertainties for $\overline{u^2}$, $\overline{w^2}$ and $\overline{uw}$ of $\pm3\%$, $\pm5\%$ and $\pm7\%$, respectively, at the lowest freestream velocity, and reduce with increasing freestream velocity. These values were estimated by comparing statistical profiles based on results from each PIV camera in isolation as well as those based on half the total number of PIV images.

A thermocouple rake was used to obtain the mean temperature profile. The rake

consisted of 14 fine-wire thermocouples covering a maximum wall-normal distance of 128.6 mm with a minimum thermocouple spacing of 4.76 mm near the wall. This spacing was doubled and then quadrupled with increasing distance from the wall. The rake was offset from the PIV laser sheet by 5 mm in the spanwise direction and placed just outside the field of view in the downstream direction. The wall-normal position of the thermocouple closest to the wall was measured using calibrated macro-photography. All thermocouples were monitored in sets of seven using a National Instruments PCI-6229 board, accurate to $\pm 1^\circ C$. Cold junction compensation of the set of seven thermocouples closest to the wall was done separately to those further from the wall, resulting in a small bias error between each set that might affect estimates of the mean temperature gradient. A small correction $(< 1^\circ C)$ was applied by symmetrically shifting each group of temperature measurements such that the temperature gradient at the location between them was equal to the average of the gradients estimated on either side (using a linear fit to the two closest thermocouples). Also, a cubic interpolation was used to extrapolate the temperature profile to the freestream for those few cases where the boundary layer was thicker than the full rake height.

The heating power input was limited to 4.1 kW, and so to obtain the highest velocity/temperature cases, the plate was allowed to reach thermal equilibrium at low speed, before increasing the velocity for the brief period during which data were acquired, taking advantage of the high thermal mass of the thick aluminum plate to keep the boundary condition approximately constant. Using this approach, the maximum drop in wall temperature during a run was $2^\circ C$, with the greatest drop near the leading edge, and the rake thermocouple nearest to the wall was seen to be stable to within $1.5^\circ C$ or 4.5% of the wall-freestream temperature difference, whichever was more strict for a given case. For the rough-wall data, the near-wall flow temperature was stable to within $1.5^\circ C$ or 3.5%.

3 Flow Conditions

To achieve a wide range of Reynolds and Richardson numbers, five free stream velocities were investigated, from $U_\infty = 1.2$ to 2.4 m/s, and for each velocity, eight isothermal wall temperatures were studied, from room temperature (approximately $26^\circ C$) to $T_w = 135^\circ C$. The resulting range of Reynolds number and Richardson number combinations are shown in figure 2. Here, $Re_\theta = U_\infty \theta / \nu_\infty$ is the momentum thickness Reynolds number, where ν_∞ is the kinematic viscosity evaluated at the freestream temperature. The displacement and momentum thicknesses for variable density flows (δ^* and θ, respectively) are defined in the usual way as

$$\delta^* = \int_0^\infty \left(1 - \frac{\rho U}{\rho_\infty U_\infty}\right) dz \quad \text{and} \quad \theta = \int_0^\infty \frac{\rho U}{\rho_\infty U_\infty}\left(1 - \frac{U}{U_\infty}\right) dz. \quad (5)$$

The mean density was computed from the temperature profile (since the pressure may be assumed constant), and the integrals were evaluated only up to the boundary layer thickness, δ. The temperature was assumed to vary linearly for the short distance from the edge of the thermocouple rake to T_∞ at δ for those cases where the boundary layer was larger than the thermocouple rake. Here, we define the boundary layer thickness
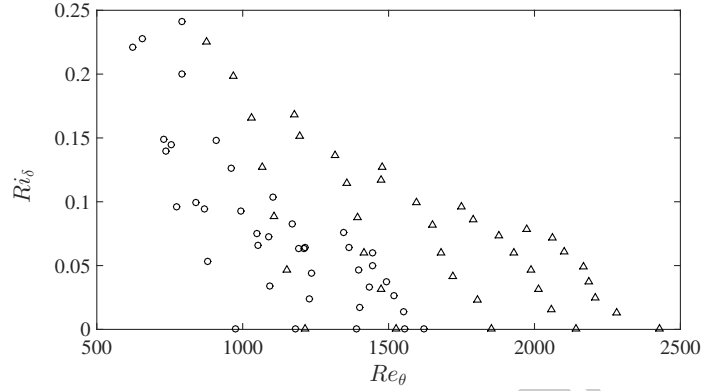
7

Figure 2: Bulk Richardson number versus momentum thickness Reynolds number for the experimental parameter space: ○ smooth. △ rough.

δ as the distance from the wall where the mean streamwise velocity is equal to its maximum value because we found a small overshoot in velocity near the edge of the boundary layer for the current experiments. The thickness according to this definition is 12-20% larger than δ_{99}, the distance from the wall at which the velocity reaches 99% of the freestream velocity. The momentum and displacement thickness values are estimated to be accurate to 2%.

For neutral stratification ($\Delta T = 0$), the Reynolds number range was $970 \leq Re_\theta \leq 1600$ (smooth wall) and $1200 \leq Re_\theta \leq 2400$ (rough wall). For the highest temperature and lowest velocity conditions, the bulk Richardson numbers approach 0.25 over both smooth and rough surfaces. From figure 2, we see that Reynolds number decreases as the stratification level increases. At the same time, the boundary layer thickness decreases due to reduced mixing, and so, for a given velocity, the Richardson number does not increase linearly with the temperature stratification.

The flow conditions for the neutral stability cases are summarized in table 1, and the flow conditions for stably stratified cases at two particular velocities are given in table 2. We choose to highlight Case V3 ($U_\infty = 1.8$ m/s) for the smooth wall, and V2 ($U_\infty = 1.55$ m/s) for the rough wall. Results at other velocities show similar trends.

In tables 1 and 2, $Re_\tau = u_\tau \delta / \nu_w$, $Re_\delta = U_\infty \delta / \nu_\infty$, $C_f = 2\tau_w / (\rho_\infty U_\infty^2)$ is the skin friction coefficient, $H = \delta^* / \theta$ is the boundary layer shape factor, and L_{uu} is the integral scale of the streamwise velocity fluctuations. The subscripts indicate the reference conditions for the fluid properties; w corresponds to wall conditions, and ∞ corresponds to freestream conditions. Also, Π is Coles's wake factor, where $\Pi = \kappa\Delta_0/2$ and Δ_0 is the maximum distance between the inner scaled mean velocity profile and the log-law in the outer portion of the boundary layer (see figure 3 for illustration). The Froude number, $Fr = U_\infty / \sqrt{g\delta_k^*}$, is defined in terms of the kinematic version of the displacement thickness,

$$\delta_k^* = \int_0^\infty \left(1 - \frac{U}{U_\infty}\right) dz \tag{6}$$

which ignores changes in fluid density and is identical to that used in incompressible

8

Case	U_∞[m/s]	δ[cm]	Re_δ	Re_θ	Re_τ	$10^3 C_f$	δ/k	δ/k_s	k^+	k_s^+	z_0^+	Π	Symbol
						Smooth							
V1	1.19	14.4	11150	976	530	3.98	–	–	–	–	0.09	0.18	○●
V2	1.50	14.3	13900	1180	644	3.68	–	–	–	–	0.09	0.20	□
V3	1.80	13.6	15900	1390	718	3.63	–	–	–	–	0.09	0.26	△
V4	2.12	13.3	18400	1550	826	3.38	–	–	–	–	0.09	0.23	◇
V5	2.36	12.8	19700	1620	886	3.46	–	–	–	–	0.09	0.20	☆
						Rough							
V1	1.23	12.8	10150	1200	623	7.54	31.4	14.09	19.9	44.2	1.23	0.36	
V2	1.55	12.8	12700	1510	787	7.66	31.4	11.93	25.1	66.0	1.84	0.42	■
V3	1.87	12.4	14900	1830	900	7.33	30.43	10.83	29.6	83.1	2.32	0.53	▲
V4	2.17	12.4	17300	2120	1060	7.48	30.43	10.30	34.7	103	2.86	0.52	♦
V5	2.46	12.2	19300	2390	1190	7.53	30.11	9.57	39.4	124	3.39	0.54	★

Table 1: Flow conditions for neutral boundary layer tests.

and isothermal flows. The Monin-Obukhov length $L^* = -u_\tau^3/(\kappa g/T_\infty Q_w)$, where $Q_w = \alpha_w \partial T/\partial z|_{z=0}$, and α_w is the thermal diffusivity of the fluid at the wall temperature. The temperature gradient at the wall is estimated using data from near-wall thermocouples (see §5.2). The Reynolds number, $Re_L = L^* u_\tau/\nu_w$ is discussed in §6. The gradient Richardson number evaluated at the wall (Ri_w) is estimated as described in §6.1.

4   Neutral boundary layer

We now examine the effects of Reynolds number and roughness on neutral boundary layer statistics so that the effects of stratification in the stable boundary layer experiments can be more clearly identified.

The mean velocity profiles for the smooth- and rough-wall neutral boundary layers are shown in figure 3. The smooth-wall cases appear as expected, with a constant wake factor of about 0.2, typical of a zero pressure gradient flow at low Reynolds numbers. The rough-wall boundary layers appear to follow the wall-similarity hypothesis of Townsend (1976), in that the effect of surface roughness is confined to the inner layer, causing a downward shift of the logarithmic profile by a distance ΔU^+ (the roughness function), as identified by Clauser (1954) and Hama (1954). The wake strength Π in the rough-wall case is somewhat larger than that seen in the smooth-wall case, which may be partly due to the increase in Reynolds number.

For the smooth-wall cases shown in figure 3, the Clauser chart method (Clauser, 1954) was used to determine the friction velocity u_τ. For the rough wall cases, the modified Clauser chart method originated by Perry *et al.* (1969) was used. Because the true position of the wall is unknown when roughness is present, three parameters were fitted: the roughness function, friction velocity, and virtual origin (referred to in the geophysical literature as the displacement height).

The friction velocity can also be estimated using the maximum total shear stress

	U_∞ [m/s]	ΔT [K]	δ [cm]	Re_δ	Re_θ	Re_τ	Ri_δ	$10^3 Ri_w$	Fr^2	δ/L^*	Re_L	H	$10^3 C_f$	L_{uu}/δ	Sym
							Smooth								
V3N		0	13.6	15900	1380	718	0	0	20	N/A	N/A	1.41	3.63	0.54	○●
V3T1		20	11.7	13600	1230	527	0.024	0.69	22	0.22	2430	1.52	3.56	0.49	□
V3T2		40	11.4	13300	1240	436	0.044	2.2	21	0.57	761	1.62	2.94	0.39	△
V3T3	1.8	60	11.0	12900	1210	358	0.064	4.8	21	1.04	346	1.74	2.43	0.37	◊
V3T4		80	10.8	12600	1170	302	0.082	8.7	21	1.58	191	1.89	2.03	0.35	▷
V3T5		100	10.8	12500	1100	240	0.102	18	20	2.66	91	2.06	1.48	0.34	◁
V3T6*		120	8.39	9800	870	149	0.093	37	24	3.32	45	2.41	1.03	0.36	▽
V3T7*		135	8.03	9400	838	146	0.098	24	22	2.14	68	2.68	1.16	0.42	☆
							Rough								
V2N		0	12.8	12700	1514	787	0	0	10	N/A	N/A	1.61	7.66	0.38	
V2T1		20	12.1	12100	1475	617	0.032	0.34	10	0.13	4890	1.71	6.07	0.36	■
V2T2		40	11.4	11500	1415	486	0.060	1.1	10	0.32	1510	1.82	4.87	0.34	▲
V2T3	1.55	60	11.3	11400	1395	402	0.087	2.6	10	0.62	652	1.93	3.90	0.29	♦
V2T4		80	11.0	11100	1360	326	0.114	5.2	10	1.01	322	2.13	3.08	0.28	►
V2T5		100	10.6	10600	1320	267	0.136	9.7	10	1.55	172	2.30	2.53	0.29	◄
V2T6*		120	9.85	9900	1200	225	0.151	15	10	2.04	110	2.51	2.34	0.30	▼
V2T7*		135	9.82	9870	1180	206	0.167	20	9	2.44	84	2.67	2.12	0.28	★

Table 2: Flow conditions for stably stratified boundary layer tests. Only the cases for $U_\infty = 1.8$ m/s (smooth) and $U_\infty = 1.55$ m/s (rough) are listed. L^* is the Monin-Obukhov length (see §5.2). An asterisk next to a case name indicates that it was subsequently found to be in the collapsed regime, where turbulent velocity statistics no longer scale with the wall shear stress.
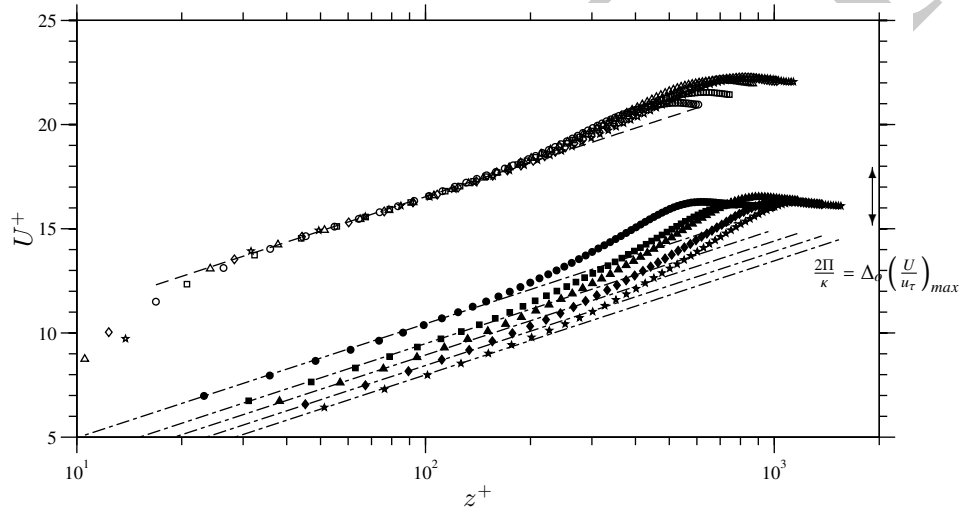
10

Figure 3: Neutral boundary layer mean velocity profiles in inner coordinates for the smooth and rough surfaces at freestream velocities from $U_\infty = 0.96$ to 2.63 m/s. Symbols according to table 1. Every other datapoint shown for clarity. $---$ Log-law with $\kappa = 0.421$ and $B = 5.6$. $\cdot - \cdot -$ Rough-wall log-law profiles, where the intercept is less than the smooth wall value by an amount equal to the roughness function, ΔU^+.
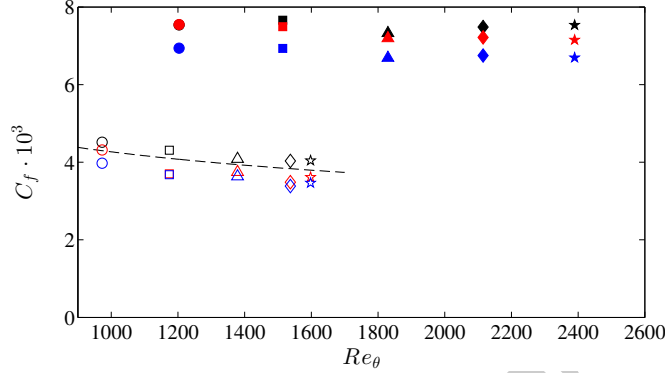
Figure 4: Neutral boundary layer skin friction variation with Reynolds number. Symbols as in table 1. Open symbols refer to smooth-wall cases and filled symbols refer to rough-wall cases. Black: Clauser chart method. Blue: total stress method. Red: Matching the peak turbulent shear stress to the estimate of Panton (1990). The low Reynolds number correlation of Smits *et al.* (1983) is shown as a dashed line.

near the wall, given by the sum of the turbulent and viscous stresses,

$$\tau_w = \rho_w u_\tau^2 \approx \left(\frac{\partial}{\partial z} (\mu U) - \rho \overline{uw} \right)_{wall}, \tag{7}$$

which for an incompressible/isothermal flow reduces to

$$u_\tau \approx \left(\nu \frac{\partial U}{\partial z} - \overline{uw} \right)_{wall}^{1/2}. \tag{8}$$

The total stress was measured at the closest point to the wall where the PIV cross-correlation windows did not overlap with the wall image. Equation 7 was used for all stratified cases while Equation 8 was only employed for neutral conditions.

For the Reynolds numbers in this study, the viscous portion of the total shear stress extends for a significant fraction of the boundary layer, and so the peak in the turbulent shear stress profile does not attain the same value as the wall shear stress. A correction can be applied using the second-order asymptotic analysis of Panton (1990) which provides an improved estimate of the friction velocity. The estimated skin-friction coefficients are compared in figure 4. Overall, the different friction velocity estimates vary by ±4.5% and ±3% for the smooth and rough neutral cases, respectively. Friction values estimated from the total stress are consistently slightly lower than those from the Clauser chart method.

The turbulent shear stress is seen to scale well with outer variables, as indicated in figure 5 where $-\overline{uw}^+ = -\overline{uw}/u_\tau^2$. A shaded region indicates the range over which the peak turbulent shear stress varies for this Reynolds number interval according to Panton (1990). As expected, the peak values do not obtain a value of unity due to the low Reynolds number. The peak smooth-wall values are somewhat lower than the Panton estimate but still within the error estimates given here and in §2. The small
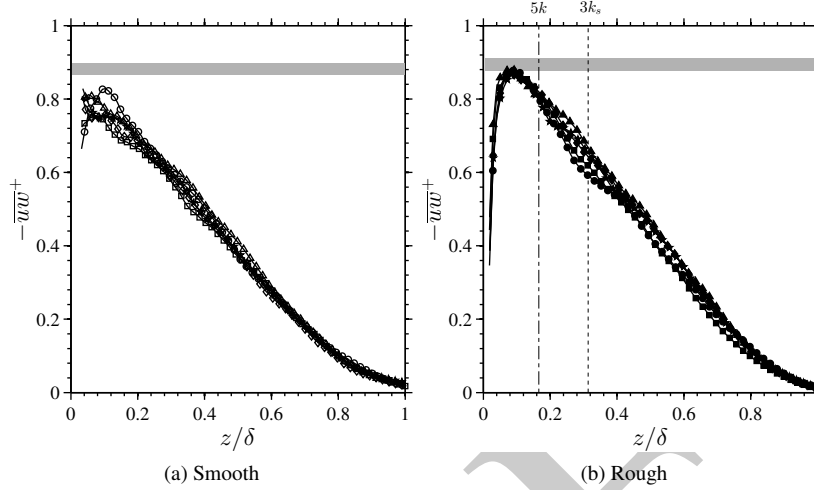
Figure 5: Profiles of Reynolds shear stress, in outer coordinates ($-\overline{uw}^+ = -\overline{uw}/u_\tau^2$). Friction velocity as determined from Clauser chart method. $\cdot - \cdot -$, $5k$; $\cdots$, $3k_s$ (shown for the highest Reynolds number case only). Shaded region indicates the range over which the peak turbulent shear stress varies for this Reynolds number interval according to Panton (1990). Every other data point is shown for clarity.

scatter in the rough-wall data is also within experimental error and does not seem to correlate with k^+. The vertical lines in figure 5b indicate the maximum extent of the roughness sublayer for the highest Reynolds number case, based on estimates of $5k$ and $3k_s$ given by Flack *et al.* (2007). Note that the $3k_s$ estimate encompasses approximately 30% of the boundary layer thickness.

The streamwise ($\overline{u^2}^+ = \overline{u^2}/u_\tau^2$) and wall-normal ($\overline{w^2}^+ = \overline{w^2}/u_\tau^2$) stresses for the smooth and rough walls are shown in figure 6. For both components, the smooth-wall profiles show excellent scaling in outer variables, well within experimental error. The results for the rough wall scale almost as well, and show the expected behavior near the wall for fully rough flows (Ligrani & Moffat, 1986). The effects of roughness appear to be confined to a region $z \leq 3k$.

5 Stably stratified boundary layer

We now examine the effects of thermal stratification. As indicated earlier, we highlight two specific cases: Case V3 ($U_\infty = 1.8$ m/s) for the smooth wall, and Case V2 ($U_\infty = 1.55$ m/s) for the rough wall (see table 2).

13

(a) Smooth - Streamwise variance

(b) Rough - Streamwise variance

(c) Smooth - Wall-normal variance

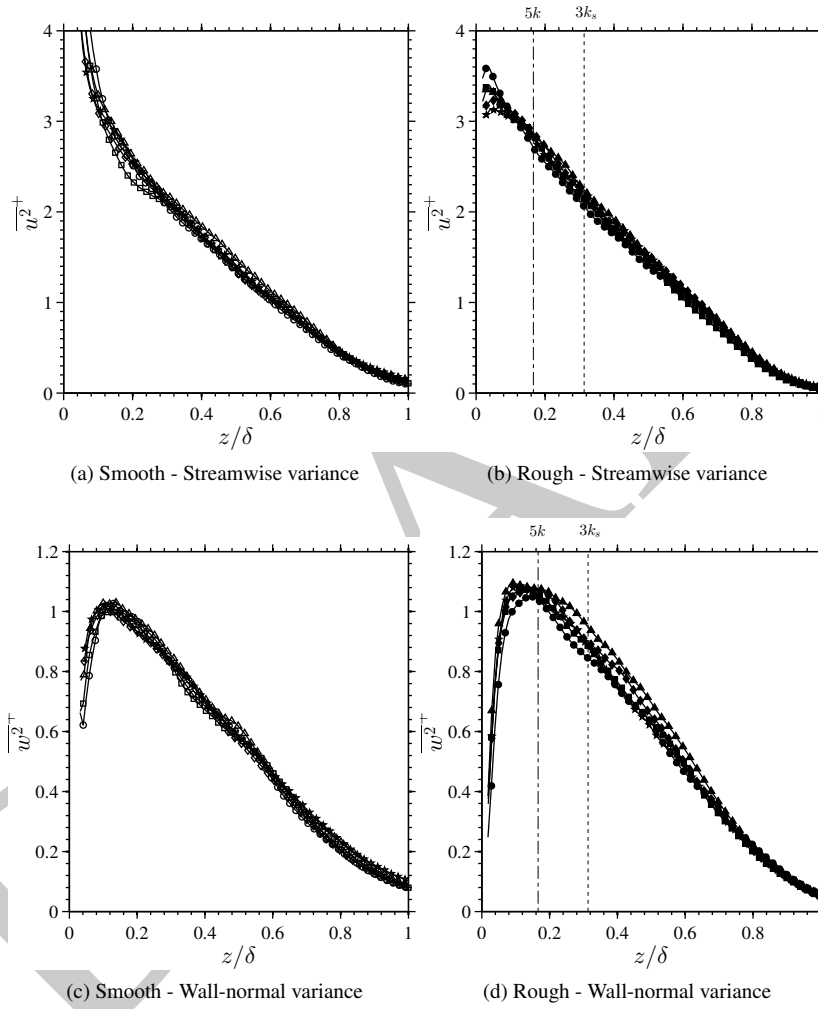(d) Rough - Wall-normal variance

Figure 6: Neutral boundary layer profiles of streamwise and wall-normal variance. Wall-normal distances of $5k$ and $3k_s$ are indicated for the highest Reynolds number case only.
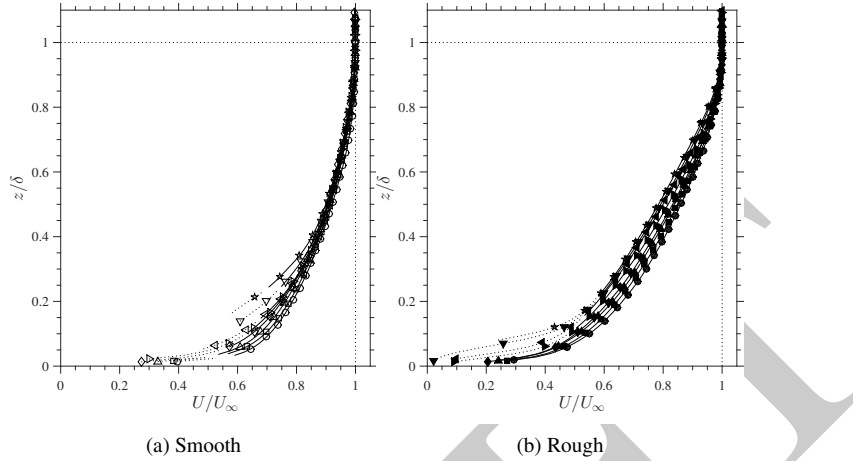
14

(a) Smooth   (b) Rough

Figure 7: Stable boundary layer mean velocity profiles: (a) smooth wall (case V3); (b) rough-wall (case V2), with varying wall-temperature. Conditions and symbols as in table 2. Symbols not shown for every wall-normal location, for clarity.

5.1 Mean flow with stratification

The mean velocity and temperature profiles for these cases are shown in outer scaling in figures 7 and 8. Dotted lines have been used to indicate data below the level at which 10% of vectors are missing due to insufficient seeding ($z_{10\%}$). Alternate vectors, corresponding to correlation peaks that satisfy the median filter, were reinserted into the data to help identify trends below this level but the data in this region must be treated with caution due the low peak ratios of many vectors.

The mean velocity and temperature layers are seen to have very similar thickness, and they display a strong reduction in wall shear and heat flux as the level of stability increases and the mixing decreases. Mean velocity profiles from the strongest stability cases resemble a laminar profile, and their shape factor, $H = \delta^*/\theta$, tends toward the laminar Blasius value of 2.59. Interestingly, the rough-wall profiles are affected by stratification throughout the entire layer, whereas the smooth-wall profiles are affected only progressively from the wall and agree well for $z/\delta > 0.45$. It will be shown that this observation helps to explain some of the differences seen between smooth and rough-wall velocity statistics.

Profiles of gradient Richardson number are given in figure 9. Temperature gradients were calculated by differentiating an exponential fit to a moving stencil of three points and then interpolating to the wall-normal locations of the mean velocity profile. Mean velocity gradients employed a nine-point stencil. This method was preferred to a central differencing scheme, which was found to be highly sensitive to the limited number of wall-normal temperature measurements. The remaining waviness in the profile is attributed to the limited number of wall-normal temperature measurements and is not thought to be physical.
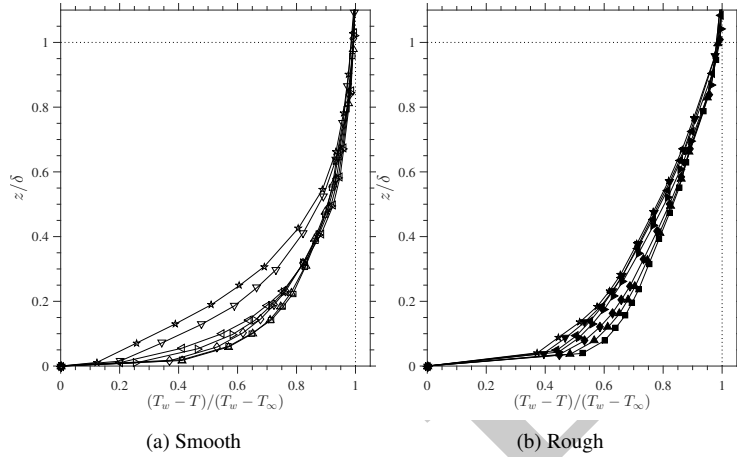
15

(a) Smooth   (b) Rough

Figure 8: Stable boundary layer mean temperature profiles: (a) smooth wall (case V3); (b) rough-wall (case V2), with varying wall-temperature. Conditions and symbols as in table 2.

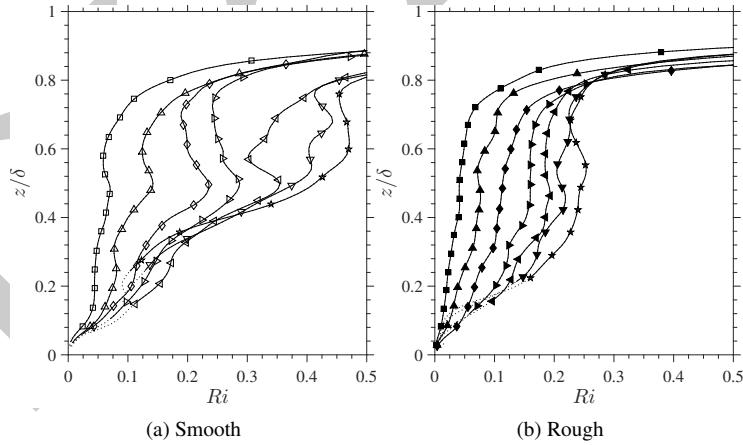
(a) Smooth   (b) Rough

Figure 9: Gradient Richardson number profile for the smooth (a) and rough (b) cases. Conditions and symbols as in table 2. Uncertainty increases significantly above $z/\delta =$ 0.7 as mean gradients become small.

16

We see that the gradient Richardson number profiles for the smooth-wall cases have a small but marked increase near $z/\delta = 0.45$ when moving away from the wall. This was the location above which the mean velocity profile was not significantly affected by stratification. The same local increase is not found in the rough-wall profiles. The bulk Richardson number for the rough-wall cases is larger than for the smooth-wall cases on average, but the gradient Richardson number, indicating local stratification, is smaller in the outer layer than for the smooth-wall cases. This observation underscores the difficulty of identifying the appropriate measure of stability in such stably stratified flows. Differences among the gradient Richardson number profiles for the four highest bulk Richardson numbers are small, but the mean profiles were seen to change sharply. This sensitivity is in accord with the large-eddy simulations of stable boundary layers by Huang & Bou-Zeid (2013) that also indicate a continuous increase in the gradient Richardson number with increasing bulk temperature differences.

The mean velocity and temperature profiles most closely follow those of Arya (1975) and Ogawa *et al.* (1985), who examined smooth-wall turbulent boundary layers developing over an isothermal plate with a uniform inflow temperature. Although these authors did not publish gradient Richardson number profiles, mean velocity and temperature profiles of similar thickness were seen to reduce in fullness with increasing stratification, in turn reducing wall shear, as seen here.

In contrast, the more recent works by Ohya *et al.* (1997) and Ohya (2001) report results that are significantly different to those seen here, despite using experimental setups similar to those used by Arya (1975) and Ogawa *et al.* (1985). For a smooth surface, Ohya *et al.* (1997) observed little change in the mean temperature profile with increasing stratification, resulting in a maximum in gradient Richardson number near $z/\delta = 0.15$ for increasing bulk stratification. For a rough surface, Ohya (2001) also observed little change in the shape of the mean temperature profile with increasing stratification. For stronger stratification, an inflection was observed in the mean velocity profiles near the edge of the boundary layer resulting in a maximum in the gradient Richardson number in the outer layer. Such differences in the mean profiles are important because Ohya *et al.* (1997) proposed that the peak in near-wall stratification led to the preferential damping of near-wall turbulence, and thereby signified the onset of a new "strongly stable" regime for higher Richardson numbers. Our results do not support the generality of that hypothesis.

Furthermore, Arya (1975) and Ohya *et al.* (1997) used the same wind tunnel facility. To obtain a wider range of stably stratified conditions, the later study operated at lower freestream velocities and thus correspondingly lower Reynolds numbers. However, the Reynolds number does not seem to be the issue because the current results compare well with the much higher Reynolds number experiments of Arya (1975), as well as the relatively lower Reynolds number experiments of Ogawa *et al.* (1985). More likely, the differences seen in the mean Richardson number profiles may be due to the different development lengths used upstream and downstream of the cold-wall section, as well as the effects of fences and other tripping devices. In addition, the widely-spaced chain roughness employed by Ohya (2001) is akin to the anomalous *d*-type roughness (Jimenez, 2004), potentially further influencing the results. Finally, the high levels of freestream turbulence (up to 4% of the freestream velocity) experienced in the experiments by Ohya *et al.* (1997) and Ohya (2001) may also have been a factor.

5.2 Monin-Obukhov length estimates

To determine the Monin-Obukhov length, the wall heat flux was estimated by calculating the gradient of the mean temperature profile near the wall using an exponential fit to the three thermocouple measurements closest to the surface, although this method is likely to underestimate the heat flux. The second thermocouple from the wall was always located at $y^+ < 44$.

The results are summarized in table 2. The bulk stability parameter δ/L^* represents the largest possible value of the stability parameter z/L^*. We see that δ/L^* increases with mean temperature difference up to value of about 2.5. This is consistent with a region of validity for MOST that shrinks with increasing bulk stratification, as discussed extensively in Mahrt (1998). Beyond making this observation, we were not able to evaluate MOST stability functions because the experimental boundary layers do not have a significant constant flux layer and the turbulent heat flux, required to evaluate the local-flux based formulation, was not measured.
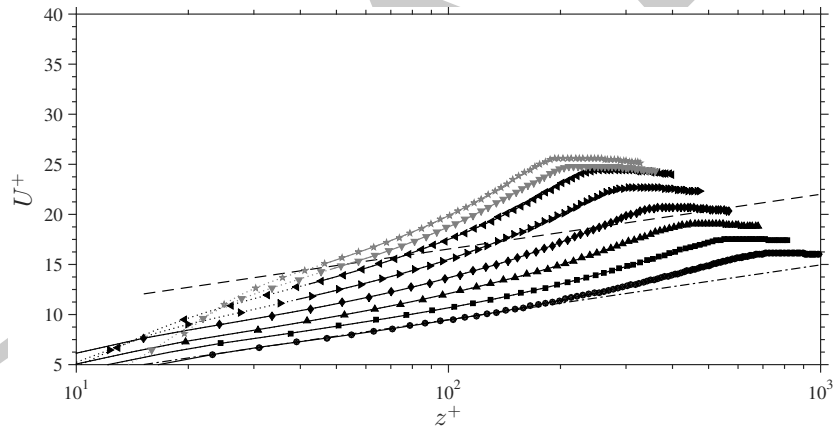
5.3 Inner scaling of mean velocity profiles

The mean velocity profiles are shown in inner scaling in figure 10, where it was assumed that the virtual origin for the rough wall (one of the three parameters required for scaling rough-wall mean velocity profiles — see §4) is the same as that found for the neutrally stratified case at the same velocity. Note that the inner length scale, ν_w/u_τ, does not vary across the layer. The friction velocity for stably stratified cases was determined from the near-wall asymptote of the total shear stress as given by equation 7 (the slope of the log-law is not known for stable flows and so the Clauser chart method cannot be used). For the smooth- and rough-wall velocities highlighted here, the friction velocity calculated using equation 7 is estimated to be accurate to $\pm 10\%$ for cases with $\Delta T < 100°C$. For the cases with the two highest wall-temperatures, the friction velocity estimates are conservatively accurate to only $\pm 40\%$ and $\pm 20\%$ for smooth and rough walls respectively, mainly because the near-wall viscous stress is a greater proportion of the total stress, and the location where 10% of vectors were missing ($z_{10\%}$) was further from the wall than the maximum turbulent shear stress as a result of deterioration in near-wall seeding quality (relatively better seeding remained near the rough wall). Grey symbols are used for these cases to acknowledge these higher levels of uncertainty, although we will show that such uncertainties will not affect our basic conclusions.

Weak stratification causes an upward shift in the log-region intercept, consistent with a thickening of the viscous sublayer. As the level of stratification increases, the profiles increase in slope and tend toward a more laminar shape. The smooth and rough wall cases follow the same trend, with a greater change for those with a smooth wall. The results are consistent with those of Arya (1975), which is the only other experimental study to examine the effect of stable stratification on mean velocity profiles in this scaling.

The increasing slope of the mean velocity profile can be highlighted by examining
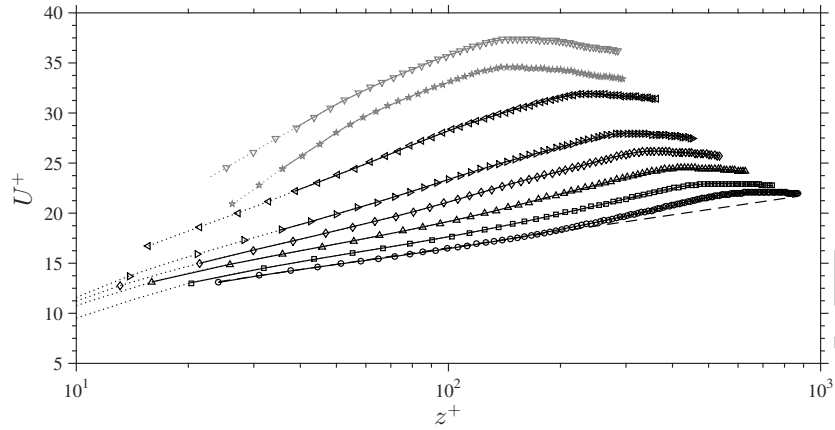
(a) Smooth

(b) Rough

Figure 10: Stable boundary layer mean velocity profiles in inner scaling for (a) smooth wall (Case V3), and (b) rough wall (Case V2). Profiles shown in grey correspond to those datasets where the estimate of u_τ has greater uncertainty due to reductions in near-wall seeding quality. Conditions and symbols as in table 2. Every other datapoint shown for clarity. $---$ Log-law with $\kappa = 0.421$ and $B = 5.6$. $\cdot-\cdot-$ Log-law shifted downward by the roughness function, ΔU^+, for neutral case.

19
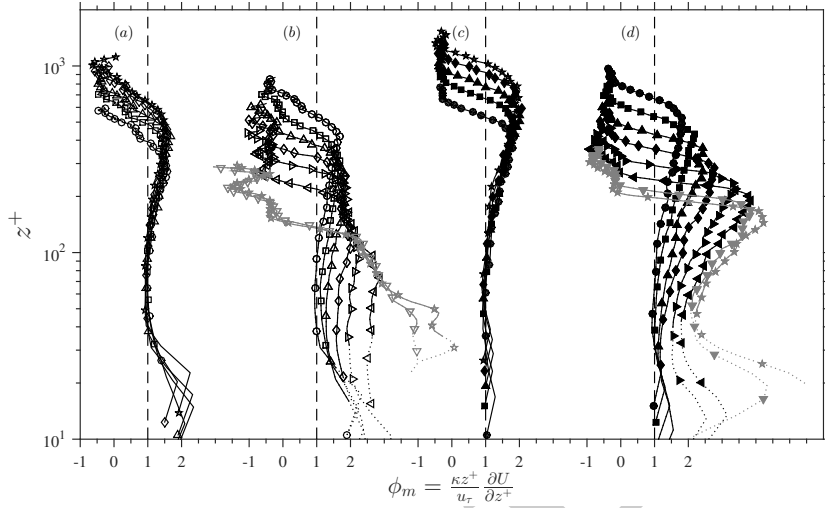
Figure 11: Normalized velocity gradient for: (a) smooth wall neutral; (b) smooth wall stably stratified; (c) rough wall neutral; (d) rough wall stably stratified cases. Symbols for neutrally stratified cases as in table 1. Symbols for stably stratified cases as in table 2.

the non-dimensional velocity gradient,

$$\phi_m = \frac{\kappa z^+}{u_\tau} \frac{\partial U}{\partial z^+},$$ (9)

which is plotted in inner coordinates in figure 11. The neutral boundary layer cases are included for comparison. Under the effect of stratification, the smooth-wall velocity profiles are seen to increase in slope by as much as a factor of 5, while the rough-wall cases increase only by a factor of 2.5 (discounting data below $z_{10\%}$, indicated with dotted lines).

More broadly speaking, the mean velocity gradient profiles invite a similarity analysis. To take into account the variations in fluid properties across the layer, we look to the van Driest transformation (van Driest, 1951, 1956) for guidance. This transformation successfully scales compressible mean velocity profiles onto the conventional log law (see Smits & Dussage (2005)). van Driest proposed that the correct friction velocity should be based on the local shear stress, which deviates from its wall value due to changes in fluid density. That is, we use a local velocity scale $u_* = \sqrt{\tau_w/\rho}$. It will be subsequently demonstrated that the turbulence profiles of the current stably stratified dataset show an improved collapse when scaling with u_*. In gradient form, the van Driest transformation suggests a similarity variable

$$\phi_m^* = \sqrt{\frac{\rho}{\rho_w}} \frac{\kappa z^+}{u_\tau} \frac{\partial U}{\partial z^+}.$$ (10)

However, the effect of stable stratification is always to increase the slope of the profile, regardless of the configuration (heating from above as in the current experiments, or
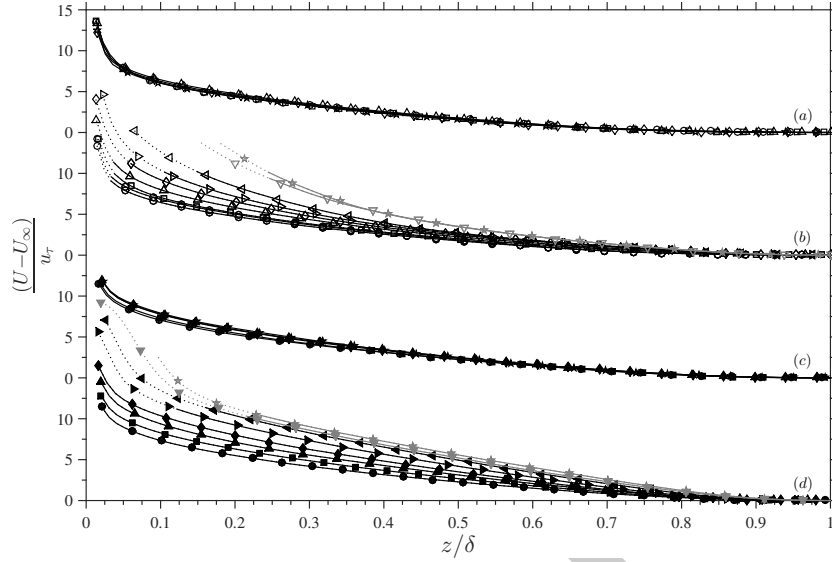
20

Figure 12: Stable boundary layer mean velocity profiles in conventional outer scaling. (a) Smooth-wall, neutral; (b) smooth-wall, stably stratified; (c) rough-wall, neutral; (d) rough-wall, stably stratified cases. Symbols for neutrally stratified cases as in table 1. Symbols for stably stratified cases as in table 2. Grey profiles signify greater uncertainty in u_τ. Every fourth datapoint shown for clarity.

cooling from below as in the study of Arya (1975)). Including the density ratio $\sqrt{\rho/\rho_w}$ in the gradient function ϕ_m will only show improved scaling for one of the two configurations, not both, and so the van Driest transformation is not appropriate for the mean velocity profiles in stably stratified boundary layers. Density weighted transformations of the wall-normal coordinate have the same problem as the van Driest transformation in this regard.

5.4   Outer scaling of mean velocity profiles

As with conventional inner scaling (using u_τ and ν_w/u_τ), the mean velocity profiles do not scale using conventional outer variables (using u_τ and δ), as shown in figure 12, and the deviations increase with increasing stratification. Such trends are expected and follow those seen by Arya (1975). However, dividing the velocity deficit by $U_\infty \delta_k^*/\delta$ instead of u_τ, as first suggested by Zagarola & Smits (1998a,b), scales the data very well (see figure 13). Here δ_k^* is the kinematic displacement thickness, that is, calculated by ignoring changes in fluid density (eqn. 6). Castillo & George (2001) showed that this scaling also worked well for boundary layers with strong pressure gradients.
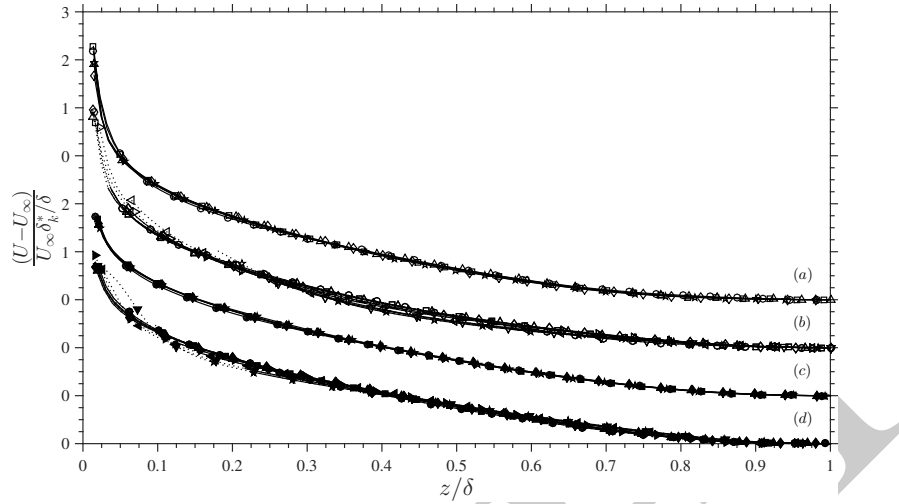
21

Figure 13: Stable boundary layer mean velocity profiles in outer layer scaling of Zagarola & Smits (1998b), using the kinematic form of the displacement thickness, δ_k^*. (a) Smooth-wall, neutral; (b) smooth-wall, stably stratified; (c) rough-wall, neutral; (d) rough-wall, stably stratified cases. Symbols for neutrally stratified cases as in table 1. Symbols for stably stratified cases as in table 2.

5.5 Turbulence profiles

Previous experimental investigations of stably stratified boundary layers have always scaled the variances using the freestream velocity, and for comparison purposes we begin in the same manner (see figure 14). As seen in the earlier studies, the turbulence intensities and shear stresses are progressively damped by increasing stability in an orderly way. The turbulent shear stress profiles retain much of their neutral shape, but the peak moves away from the wall slightly with increasing stratification, which is consistent with a thickening of the near-wall buffer region as found for the mean velocity profiles shown in figure 10. The near-wall results should be treated with some caution since the near-wall seeding level deteriorated at the higher levels of stratification. Nevertheless, the peak in the turbulent shear stress has been captured for all but the two strongest stratification cases, for both smooth and rough walls.

The increasing damping of turbulence by stability seen here follows the trends seen by Arya (1975) and Ogawa *et al.* (1982), and in the weaker stability cases examined by Ohya *et al.* (1997) and Ohya (2001). At larger levels of stratification, however, Ohya *et al.* (1997) and Ohya (2001) observed a preferential collapse of near-wall turbulence at a critical Richardson number, which they interpreted as signaling the start of a strongly stable regime, with this near-wall collapse as its defining characteristic. No preferential collapse of near wall turbulence is observed in the current experiments. Rather, we see an orderly decrease in the turbulence across the boundary layer in this scaling, with a greater degree of damping in the outer layer than in the near-wall region.

In an effort to discriminate between the (coupled) effects of Reynolds and Richard-
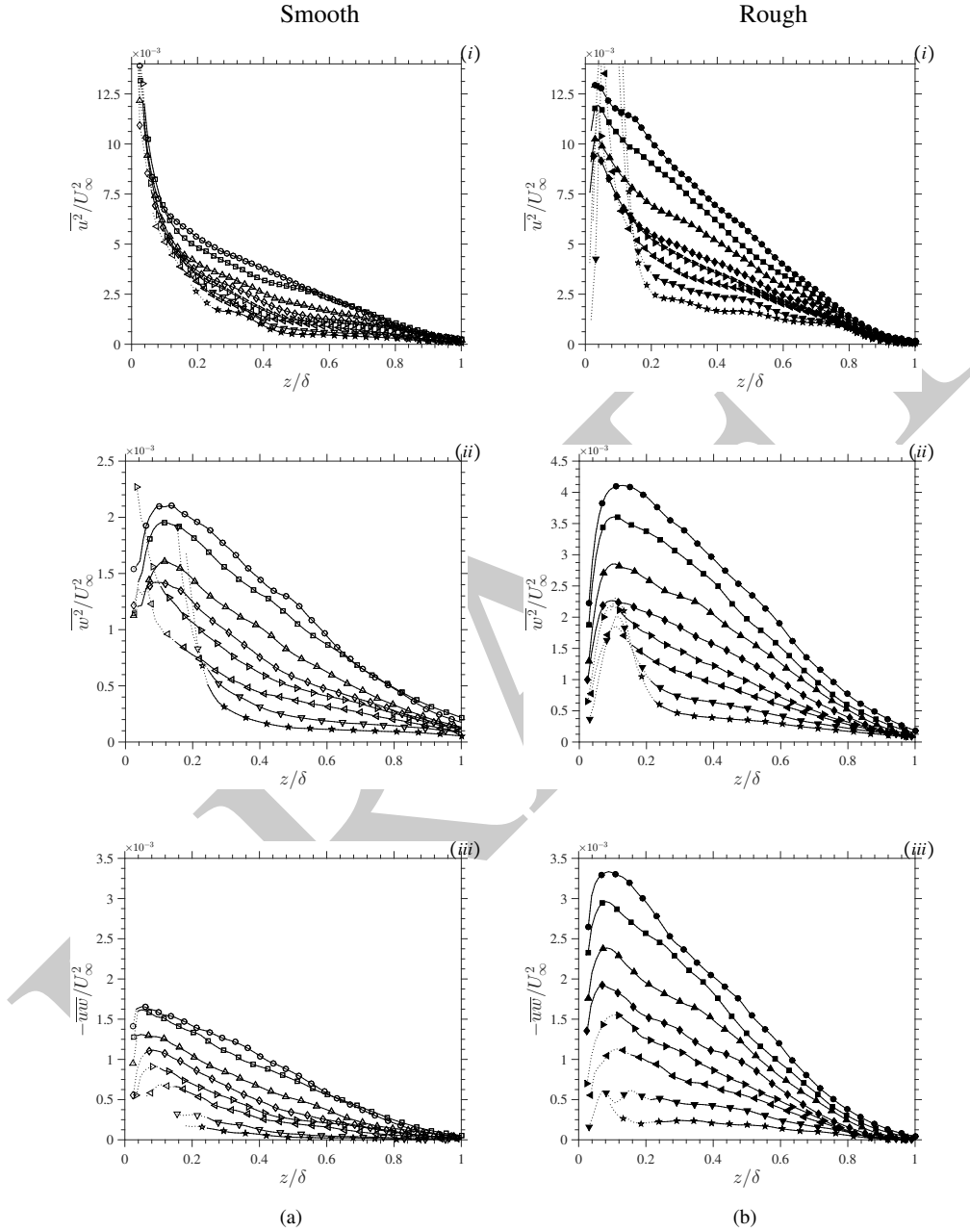
Smooth

Rough

Figure 14: Turbulent stresses scaled by freestream velocity for (a) smooth (Case V3), and (b) rough walls (Case V2). Near wall data below $z_{10\%}$ shown with dotted lines. Conditions and symbols as in table 2.

23
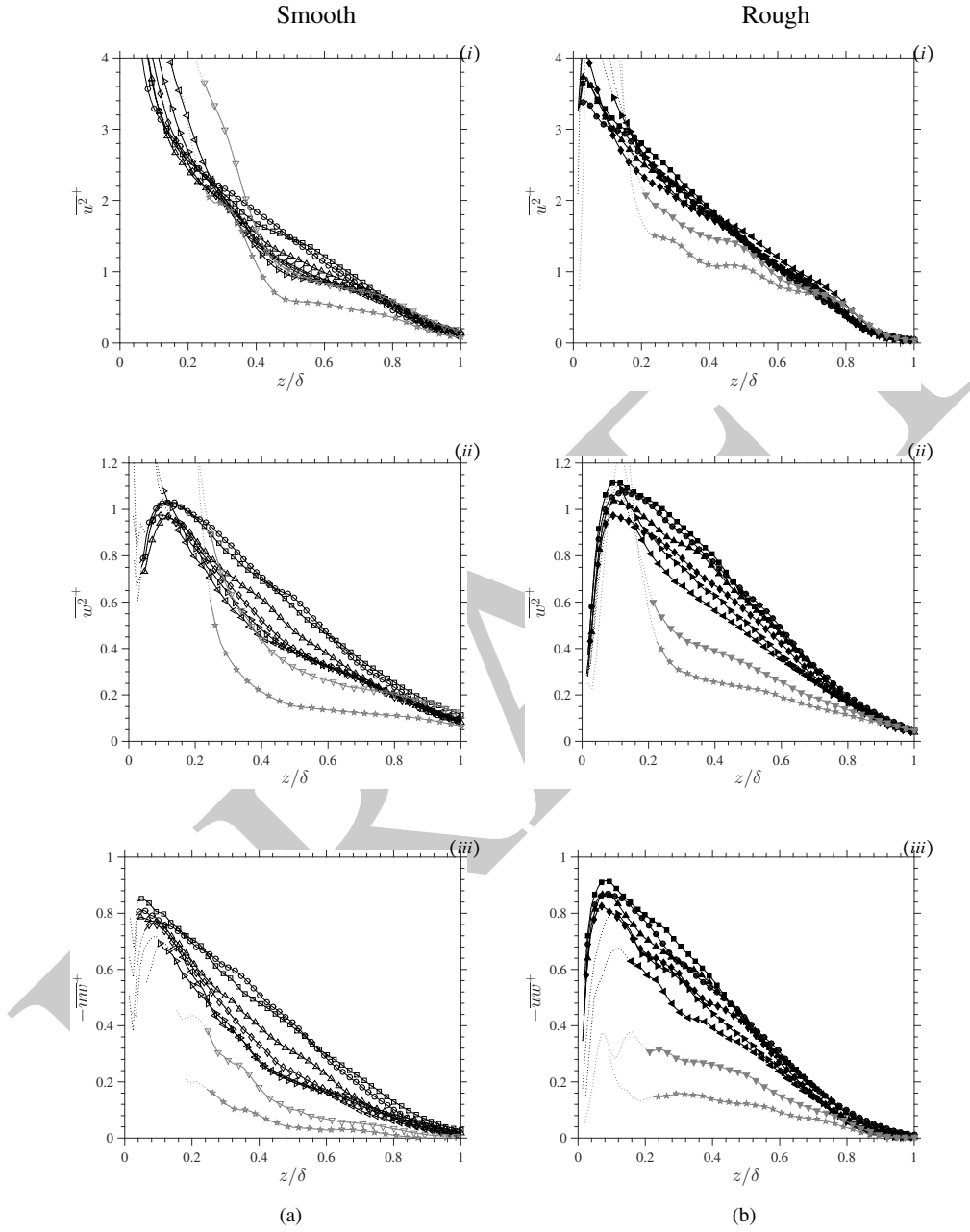
Smooth   Rough

Figure 15: Turbulent stresses in outer layer scaling for (a) smooth (Case V3), and (b) rough walls (Case V2). Near wall data below $z_{10\%}$ shown with dotted lines. Cases where $z_{10\%}$ lies significantly farther from the wall than the peak stress are shown in grey. Conditions and symbols as in table 2.

son number, we now present the turbulence profiles in conventional outer layer scaling (see figure 15), in the expectation that this will account for Reynolds-number effects. As for the mean velocity profiles, the friction velocity was determined for all stratified cases using the near-wall maximum of the total shear stress (Eq.7) as the Clauser chart method could not be used for these cases. If we disregard the two highest wall-temperature cases for now, the turbulence profiles show improved agreement in this scaling compared to that using the freestream velocity (figure 14). We see that for smooth and rough walls the peaks in the turbulent shear stress and the wall-normal turbulence decrease slowly with increasing stratification. The thickening of the viscous sublayer, seen in the mean velocity profiles, is also apparent in the profiles of streamwise variance for the smooth wall (figure 15a(i)), where the peak in near-wall turbulence moves away from the wall. For the rough-wall cases (figure 15b), the growth in the peak in $\overline{u^2}$ is clear in this scaling, suggesting that the buffer layer is no longer completely subsumed by the roughness sublayer for the cases with the strongest stratification. It may be that under these conditions the flow can no longer be considered fully rough (Ligrani & Moffat, 1986).

Only small changes in profile shape are noted for those cases where the peak shear stress scales with the wall stress. A slight kink is observed at $z/\delta = 0.45$ for the strongest stratifications in the smooth-wall data that is not present in the rough-wall data. This kink is visible in the streamwise and wall-normal variances as well as in the turbulent shear stress. In contrast, the rough-wall profiles show no such localized change in slope. The location of the kink in the smooth-wall data suggests a connection with the mean velocity profile, which was primarily affected by stratification below $z/\delta = 0.45$ for the smooth wall, whereas the effect of stratification was noticeable throughout the entire boundary layer for the rough wall. Similarly, the local gradient Richardson number profiles show a slight increase at $z/\delta = 0.45$ for the smooth-wall data, whereas the rough wall profiles increase more evenly. It appears that the local stratification profile has a small but marked effect on the shape of the wall-normal turbulence profiles.

To explore the effects of fluid property variations, we can use a density-weighted scaling as used in compressible flow, where Morkovin (1961) hypothesized that "the essential dynamics of compressible shear flows follow the incompressible pattern" and are therefore expected to scale with variations in the local fluid density, provided the dynamic effects of density fluctuations can be neglected. Under these conditions, the turbulent stresses ($\rho\overline{u^2}$, $\rho\overline{w^2}$, $-\rho\overline{uw}$, etc.) should scale with the wall shear stress, τ_w. In effect, this modifies the local friction velocity scale to become, $u_* = \sqrt{\tau_w/\rho} = \sqrt{\rho_w/\rho}\, u_\tau$. Figure 16 demonstrates that this Morkovin scaling improves the agreement of the profiles, especially near the wall. The scaling of the smooth-wall streamwise stresses in the middle of the layer is also seen to be improved.

The success of the Morkovin scaling for cases with weaker stratification suggests that similar conclusions can be drawn about the structure of weak to moderately stable boundary layers as are regularly drawn for compressible boundary layers since turbulence intensity is seen to reduce proportionally to the change in the wall shear stress and the effects of stratification are seen to be confined to small changes in the profile shape shape that appear correlated with the changes in mean stratification. The

25

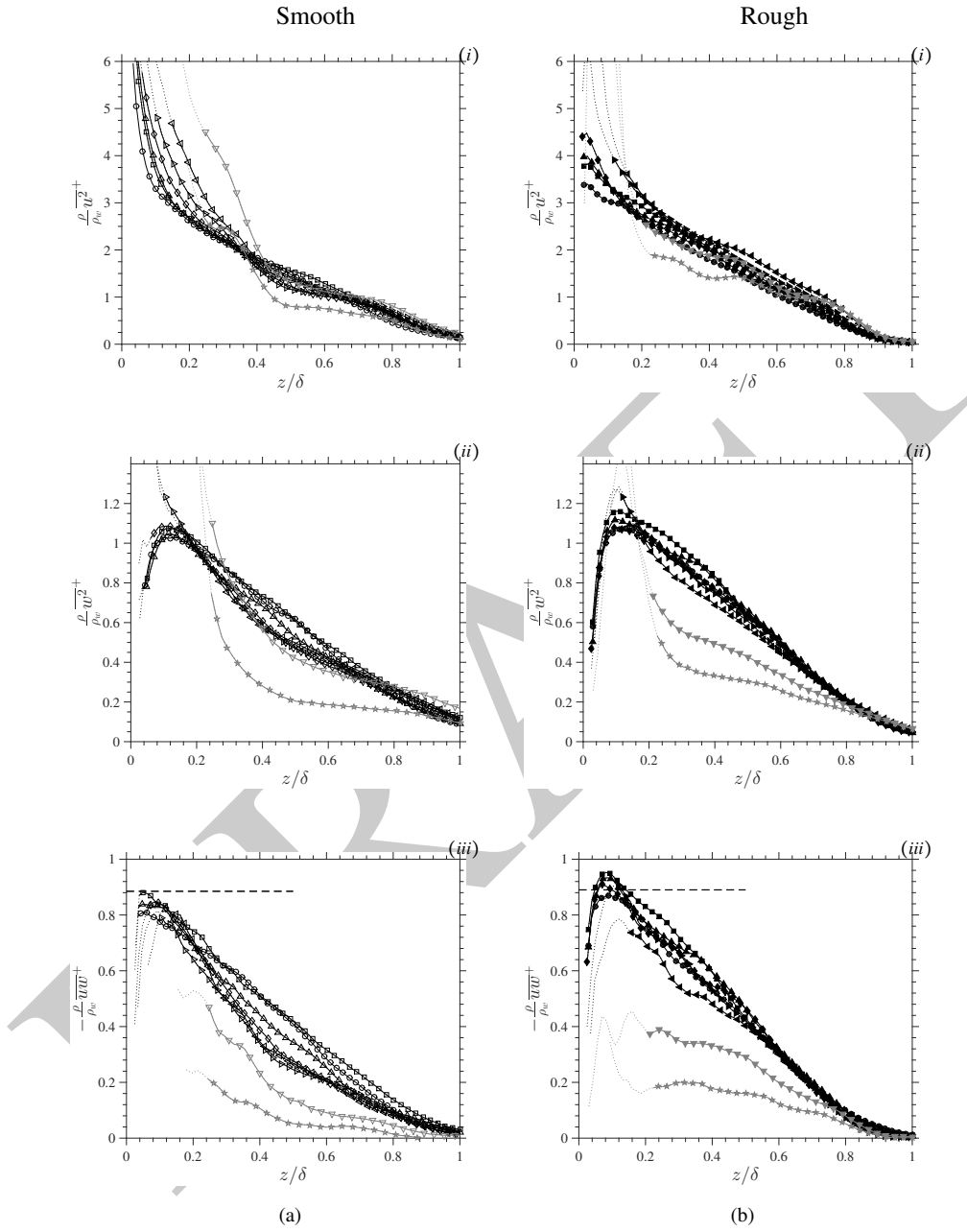Smooth   Rough

Figure 16: Turbulent stresses in density-weighted (Morkovin) outer layer scaling for smooth (a) and rough walls (b). Near wall data below $z_{10\%}$ shown with dotted lines. Cases where $z_{10\%}$ lies significantly farther from the wall than the peak stress are shown in grey. Conditions and symbols as in table 2. Horizontal dashed line indicates the magnitude of the near-wall shear stress peak for the neutrally stratified case as predicted by Panton (1990).

26

implications are two-fold: dilatation effects do not appear to be important in the current experiments, despite large changes in density, and the turbulent structure of the boundary layer remains unchanged up until some critical stratification at which point the turbulence collapses and no longer scales with the wall shear.

Note that u_* is defined in the same way as the velocity scale used in the "local scaling" of Nieuwstadt (1984; 1985) since $u^{*2} = (\rho_w/\rho)u_\tau^2 = \tau_w/\rho = -\overline{uw}$. The underlying arguments, however, are different because Morkovin scaling does not incorporate gravity or the turbulent heat flux, both a part of Nieuwstadt's formulation. Instead, Morkovin scaling can be thought of as the appropriate scaling to account for variations in Reynolds number in a fluid of variable density where buoyancy effects on turbulent structure are negligible.

5.6 Anisotropy

The ratio of rms velocity fluctuations in the streamwise and wall-normal directions, that is the anisotropy ratio σ_w/σ_u, is shown in figure 17. The results support the suggestion that the structure of turbulence is relatively insensitive to stratification for all but the two cases with the highest wall temperatures. The anisotropy ratio is insensitive to Reynolds number for both smooth- and rough-wall cases, with an almost constant value of approximately 0.6 over much of the layer, increasing toward the isotropic value of unity near the edge of the boundary layer, in line with the observations of Aubertine & Eaton (2005). The anisotropy ratio only reduces significantly as the turbulence begins to collapse and no longer scales with wall shear, a behavior that is consistent with the flattening of turbulent structures and dampening of the wall-normal momentum transport. These results agree with the atmospheric measurements by Kaimal *et al.* (1972), who observed changes in the ratio of the wall-normal to streamwise velocity spectra for $z/L \to 1$, which in our case would occur in the outer layer for the cases with the strongest stratification, where we also see changes in anisotropy.

The relative insensitivity of the anisotropy parameter to weak stability was also noted and discussed by Arya (1975). Stable stratification extracts energy directly from the $\overline{w^2}$ and $-\overline{uw}$ stresses but $\overline{u^2}$ is also reduced by the interaction of $-\overline{uw}$ and the mean velocity gradient. Previous direct numerical simulation studies have suggested that the reduction in the shear production of $\overline{u^2}$ is more important than the buoyant damping of $\overline{w^2}$ (Shah & Bou-Zeid, 2014). Through the action of the pressure fluctuations, the energy is redistributed among all three components, explaining the relative insensitivity of this parameter to stratification. Similar conclusions can be drawn from the ratios of the streamwise and wall-normal stresses with the turbulent shear stress, also shown in figure 17. These results underline the marked decrease in turbulent transport efficiency as stability increases to levels that result in departures from wall shear-stress scaling.

5.7 Collapse

When we now consider the two strongest stratification cases, we see that in either conventional outer scaling or in Morkovin scaling these cases exhibit a sudden and drastic reduction in turbulence levels. The shape of the profiles also depart significantly, indicating that this collapse is not simply due to increased uncertainty in the friction
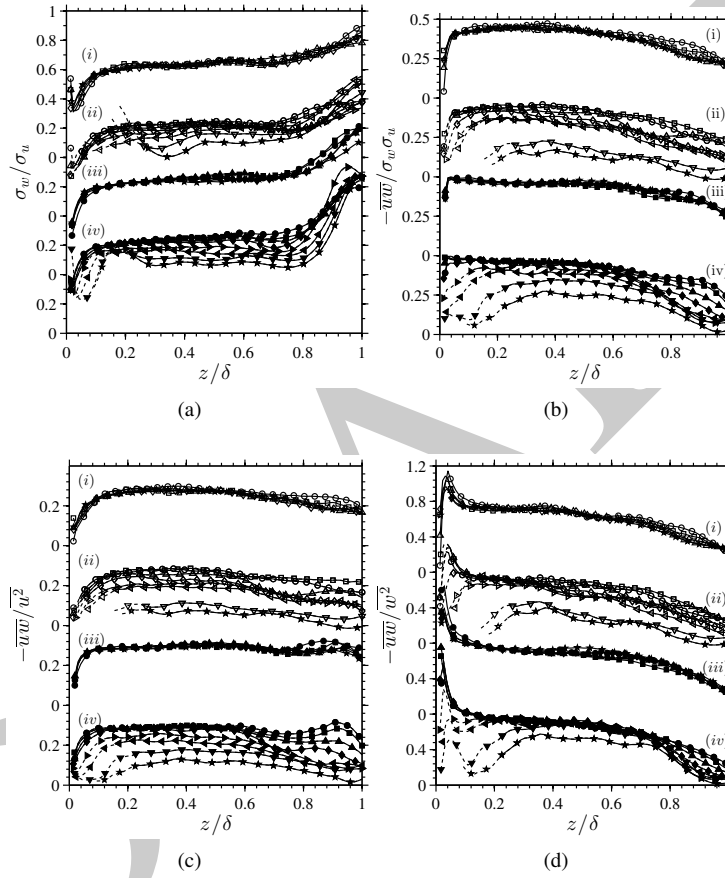
Figure 17: Evolution of ratios of the turbulent stresses with wall-distance. (i) Smooth wall neutrally stratified (ii) smooth wall stably stratified (iii) rough wall neutrally stratified (iv) rough wall stably stratified cases. Symbols for neutrally stratified cases as in table 1. Symbols for stably stratified cases as in table 2.

28

velocity. The absence of preferential damping of near-wall turbulence in either scaling for the highest stability cases is again noted. This departure is seen to occur for bulk Richardson numbers exceeding 0.1 for the smooth wall, and about 0.15 for the rough wall. These values do not change significantly with freestream velocity, although the range of Reynolds numbers is small, and a weak Reynolds number dependence is not precluded. Ogawa *et al.* (1985) observed the collapse of turbulence intensities for a smooth wall at similar bulk Richardson and Reynolds numbers as in the current study. Once the turbulence collapses, the remaining fluctuations are weak, patchy and not continuous. Nevertheless, the instantaneous PIV velocity fields (not shown here) indicate that weak individual hairpin structures persist even at the highest levels of stratification.

5.8   Quadrant Analysis

We have found that increasing stratification is associated with strong reductions in turbulent shear stress, leading to the collapse of turbulent production by mean shear. To explore this process more closely, we examine the quadrant contributions to the turbulent shear stress in the *u-w* plane, as formalized by Lu & Willmarth (1973). The results are presented in figure 18 in outer scaling. The motions that contribute to negative shear stress and positive turbulence production by mean shear, commonly termed ejections (Q_2) and sweeps (Q_4), are seen to be most affected by stratification, whereas the contributions to positive shear stress and negative production (Q_1 and Q_3) are unaffected (relative to the local wall shear stress). At the same time, the effect on positive production motions is asymmetric, with ejections damped to a greater extent than sweeps. This is demonstrated more conclusively by examining the ratio of their contributions, as in figure 19, where we see that the greatest changes in their relative magnitude occurs in the outer layer. This ratio was found to be insensitive to changes in Reynolds number, at least for the neutral boundary layer (not shown here).

   The quadrant analysis thus suggests a weakening of turbulent motions that contribute to the production of turbulence, such as hairpin vortices. These vortices are inclined in the downstream direction, inducing ejections between the legs of the vortex and sweeps outside the legs. As hairpin vortices convect with a velocity close the local mean value (Adrian *et al.*, 2000), quadrant analysis can be interpreted as revealing motions induced by a mean hairpin vortex at a given wall normal location. As ejections originate closer to the wall than a given hairpin head they must overcome a stronger temperature gradient than sweeps which originate further from the wall, potentially explaining our observed bias toward the damping of ejections.

5.9   Richardson number scaling and comparisons with the atmospheric surface layer

We now compare our results to those in the stable atmospheric surface layer, especially with respect to possible Reynolds number discrepancies. A number of different scaling systems have been proposed. The most renowned is MOST, which employs the fluxes of heat and momentum, and the buoyancy parameter β ($= g/T_0$) as the primary governing variables (Monin & Obukhov, 1954). More recently, combinations of wall-normal velocity variance, temperature variance, wall-normal position (Sorbjan, 2010) or the
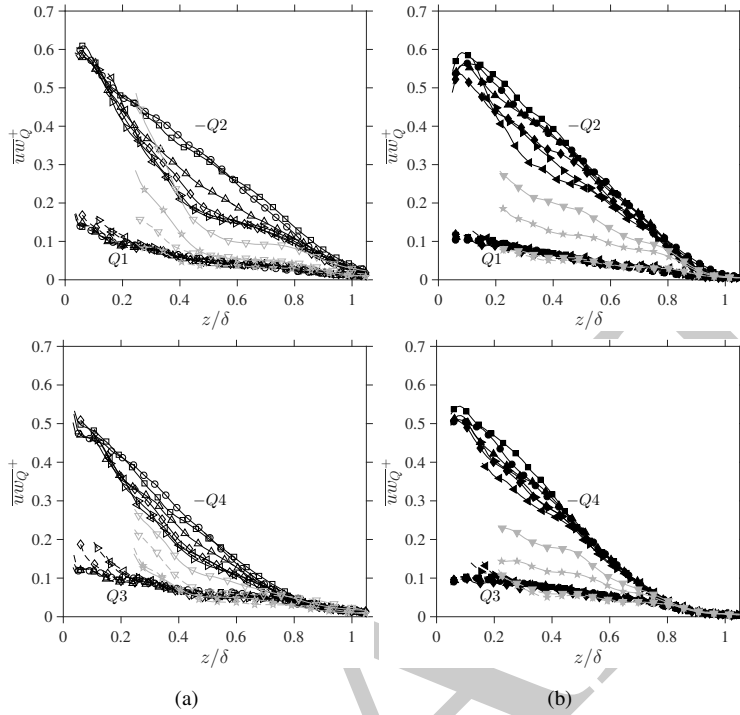
Figure 18: Quadrant contributions to the turbulent shear stress for (a) smooth- and (b) rough-wall flows. Conditions and symbols as in table 2. Grey profiles indicate those cases for which their is significantly greater uncertainty in the estimate of u_τ.
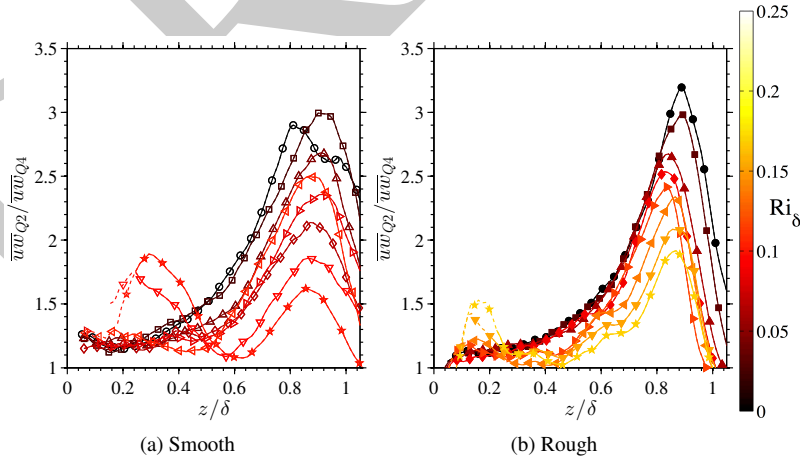

Figure 19: Ratio of $Q2$ and $Q4$ contributions for (a) smooth- and (b) rough-wall flows. Neutrally stratified conditions from table 1. Thermally stratified conditions from table 2.

dissipation of TKE (Grachev *et al.*, 2015) have been combined with the Brunt-Väisälä frequency and β to create new scaling systems. Of these, we choose to compare our results with those from the stable atmosphere in the gradient scaling of Sorbjan (2010), where the velocity, temperature and length scales are defined in terms of the local temperature gradient, the buoyancy parameter, and the wall-normal distance. Newer formulations may be more advantageously constructed (see, for example, the discussion by Grachev *et al.* (2015)), but the gradient-based formulation allows for a comparison with atmospheric results using variables that were measured in the current experiments (we do not have access to, for instance, accurate estimates for the dissipation rate or the turbulent heat flux).

In Sorbjan's scaling the dependent variables, such as the turbulent shear stress and wall-normal variance, become functions of the gradient Richardson number. That is,

$$\frac{-\overline{uw}}{U_s^2} = G_t\left(Ri\right) \qquad\qquad \frac{\overline{w^2}}{U_s^2} = G_w\left(Ri\right), \qquad\qquad (11)$$

where the relevant velocity scale is $U_s = l_0 N$ and l_0 is the mixing length. Sorbjan's formulation employed two velocity components to account for rotation of the mean velocity direction due to Coriolis forces, but is similar to that shown here in any horizontal plane. Sorbjan's scaling is consistent with MOST as the Richardson number is a function of z/L in this theory. Sorbjan originally proposed that the mixing length increases linearly with wall-normal distance, that is, $l_0 = \kappa z$. This scaling will fail further from the surface where the mixing length grows more slowly. Hence, Sorbjan (2012) suggested employing the mixing length model of Blackadar (1962) such that $l_0 = \kappa z/(1 + \kappa z/\lambda)$ where λ is an external parameter usually modeled in terms of the Coriolis parameter and Rossby number.

Sorbjan (2010) verified this gradient-based scaling using data from the Surface Heat Budget of the Arctic Ocean (SHEBA) experiment (Grachev *et al.*, 2008). The gradient Richardson number was chosen so that $0.5 Ri_e < Ri < 2 Ri_e$, where Ri_e is the value of the gradient Richardson number predicted from the MOST similarity functions established by Grachev *et al.* (2007, 2008), thus ensuring that the gradient-based results correspond closely to MOST. The wall-normal and shear stress data of Sorbjan (2010) are shown in figures 20 and 21. Solid black lines indicate best-fit functions to the atmospheric data as given by Sorbjan (2010). While the original study of Sorbjan (2010) did not account for the wall-normal dependence of the mixing length, the data points represent the mean value for a small Richardson number bin, effectively averaging out any wall-normal dependence (within measurement error). The data of Sorbjan (2010) were therefore found to provide the same empirical trends as the more complete scaling proposed by Sorbjan (2012), which accounted for the wall-normal dependency directly. The comparison between atmospheric and experimental results using the data of Sorbjan (2010) thus remains valid. The power-laws observed at low Ri are consistent with classical eddy viscosity/diffusivity models (sometimes known as K-theory). The high Ri power-laws are empirical. As Sorbjan (2010) pointed out, the error associated with this atmospheric data increases with Ri.

The results for the stably stratified cases listed in table 2 are also shown for the interval $z^+ > 40$ and $z/\delta < 0.7$ (subject to $z > z_{10\%}$), chosen to avoid regions with
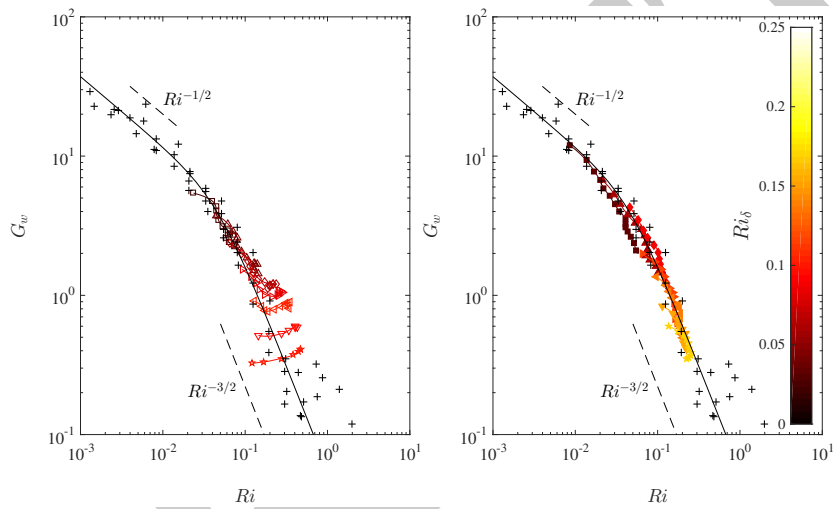
31

Figure 20: Wall-normal velocity rms in the gradient based scaling of Sorbjan (2010) as a function of gradient Richardson number. (a) Smooth and (b) and rough wall symbols and conditions as in table 2. Data shown between $z^+ > 40$ and $z/\delta < 0.7$ and $z > z_{10\%}$. All data from the present wind tunnel measurements are colored by bulk Richardson number (Ri_δ). The solid line corresponds to the empirical correlation of atmospheric data (+) presented by Sorbjan (2010).
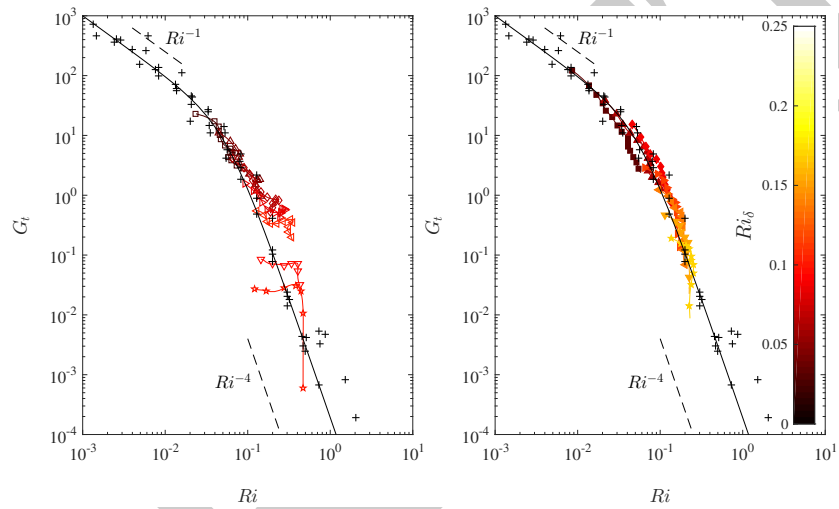
Figure 21: Turbulent shear stress, $\overline{uw}$, in the gradient based scaling of Sorbjan (2010) as a function of gradient Richardson number. (a) Smooth and (b) and rough wall symbols and conditions as in table 2. Data shown between $z^+ > 40$ and $z/\delta < 0.7$ and $z > z_{10\%}$. All data from the present wind tunnel measurements are colored by bulk Richardson number (Ri_δ). The solid line corresponds to the empirical correlation of atmospheric data (+) presented by Sorbjan (2010).

33

significant viscous effects and where small gradients cause large uncertainties in the gradient Richardson number. The mixing length model of Blackadar (1962) was used, as suggested by Sorbjan (2012). The external parameter, λ, is conventionally modeled for the atmosphere in terms of the Coriolis parameter and Rossby number; an approach which is not valid for the current experiments. In the absence of better information, we choose λ to be the integral length scale of the streamwise velocity fluctuations, L_{uu} for the data shown in figures 20 and 21 (see table 2). Despite the large field of view of the current experiments, it was necessary to fit exponential tails to the autocorrelation of velocity for large separations in order to obtain a more accurate estimate of the integral length. Williams (2014) gives further details.

We see that within the experimental uncertainty our results agree well with the atmospheric data prior to collapse (small to moderate Richardson numbers). This is especially true for the rough wall. The smooth-wall data diverge significantly only when the collapse of turbulent production is imminent, however the post-collapse rough-wall data continue to correspond closely to the trends of Sorbjan. The smooth-wall collapsed cases show a drop in scaled shear stress within the outer layer at high Richardson number but this is within the uncertainty of Sorbjan's original study. This region is also the most sensitive to choice of mixing length model although using a linear model instead of that of Blackadar only caused deviations that are once again within the uncertainty of the atmospheric data. Other choices for λ were also investigated, such as the streamwise integral length scale of the wall-normal velocity fluctuations L_{vv}, but they did not provide any particular improvement. Scatter of the higher stability smooth-wall data around the atmospheric correlation for the strongest stabilities may be the result of a small remaining dependence on wall-normal position not captured by Blackadar's mixing length model.

The wide range of wall-normal positions over which agreement is observed suggests the broad validity of gradient-based and semi-local MOST scalings outside any region affected by viscosity. This promising correspondence also supports the proposal that wind-tunnel studies of stable boundary layers at low Reynolds number can yield results that can be directly applied to the understanding of the atmospheric surface layer.

To this end, we examine the wall-normal fraction of TKE, $A_w = \sigma_w^2/(\sigma_u^2 + \sigma_v^2 + \sigma_w^2)$, which is is often modeled as a function of stability parameters z/L or Ri (Schumann & Gerz, 1995; Zilitinkevich $et\ al.$, 2013). We have no measurements of the spanwise component of turbulence, but we can make an estimate from a fit to the spanwise proportion of the turbulent kinetic energy A_v given by Sorbjan (2010), resulting in an estimate, A_w^*. The results are shown in figure 22, along with the atmospheric data of Sorbjan (2010) (A_w does not involve the mixing length and so a correction for wall-normal distance is not required). Our data correspond approximately with those of Sorbjan (2010), who found a slight increase in A_w above the neutral value for small to moderate Richardson numbers, before decreasing rapidly as wall-normal turbulence is suppressed at higher stability levels. The sharp increase in A_w^* seen at the highest Ri of each set is likely due to the increasing influence of measurement noise toward the edge of boundary layer as the stresses become small. The current experiments suggest a dependence on wall-normal distance, in addition to a dependence on Richardson number.
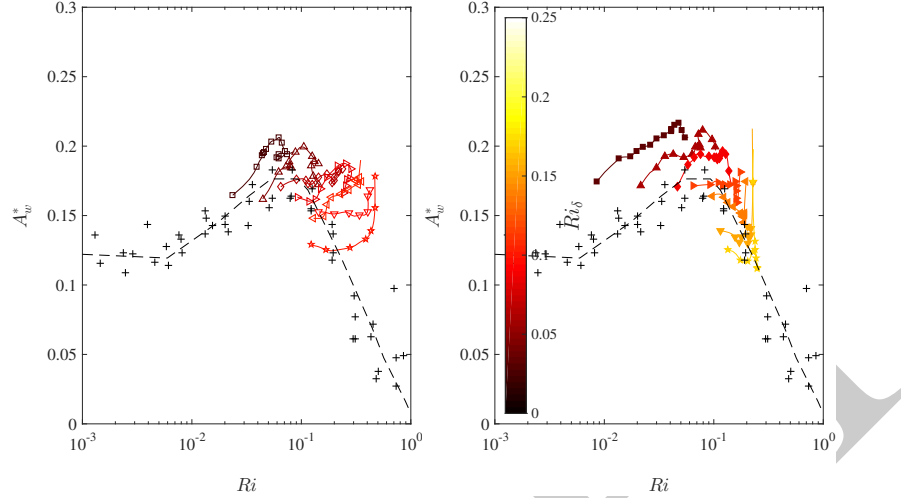
Figure 22: Estimate of the wall-normal proportion of the turbulent kinetic energy, $A_w^* = \sigma_w^2/(\sigma_u^2 + \sigma_v^2 + \sigma_w^2)$. (a) Smooth and (b) and rough wall symbols and conditions as in table 2. Spanwise variance was estimated from A_v correlation of atmospheric data by Sorbjan (2010). Data shown between $z^+ > 40$ and $z/\delta < 0.7$ and $z > z_{10\%}$. All data from the present wind tunnel measurements are colored by bulk Richardson number (Ri_δ).

6   Critical stratification

It was noted in §5.5 that for weak to moderate stability, turbulence intensities scale with the local shear stress and that the turbulent structure was insensitive to stability. For the cases with the strongest stratification, however, turbulent production was not sustained, as indicated by large changes in profile shape and departures from Morkovin scaling. These observations indicate the onset of a stability regimes where the local turbulence is no longer able adjust to changes in the local wall shear stress. We have used the term "collapsed" to denote this regime to avoid confusion with previous definitions of a "strongly stable" regime.

A number of measures have been proposed in the literature to delineate the collapse of turbulence and delineate stability regimes. The most common measure (experimentally) is the critical bulk Richardson number, determined in this study to be approximately 0.1 and 0.15 for smooth and rough surfaces, respectively. No dependence on freestream velocity was seen in the current dataset, although the limited Reynolds number range does not preclude this possibility. The observed sensitivity to surface roughness (and possibly Reynolds number) means that the bulk Richardson number is not a suitable parameter for consistent delineation of these two regimes.

In this respect, Flores & Riley (2011) have suggested that Reynolds number based on the Monin-Obukhov length and the friction velocity provides a better measure of the collapse of turbulence. They observed collapse for $Re_L = Lu_\tau/\nu_w \lesssim 100$ in simulations of turbulent open channel flow, suggesting that collapse occurs when the dynamic sub-

layer is not large enough to sustain a buffer region. Collapse was observed in the current experiments for $Re_L \lesssim 130 \pm 60$, based on estimates of the Monin-Obukhov length using the method described earlier. The Reynolds numbers based on wall-temperatures on either side of collapse were averaged to obtain this estimate, and the error bound takes account of this averaging and variations between cases at different velocities. Given that Reynolds number drops precipitously prior to collapse and then decreases more slowly, this estimate may be biased to larger values. We conclude, therefore, that the current experiments are consistent with the bound in critical Monin-Obukhov Reynolds number suggested by Flores & Riley (2011). We did not observe any influence of wall roughness on this bound. For the current dataset, the parameter L^*/k varied between 3 and 11 immediately after collapse, and it increased with tunnel flow velocity.

6.1 Stability theory of Schlichting

The linear stability analysis by Schlichting (1935) identified the gradient Richardson number evaluated at the wall, Ri_w, as the parameter that separates regimes where small disturbances would grow or decay. The critical value of Ri_w depends primarily on Reynolds number ($Re_{\delta_k^*} = U_\infty \delta_k^* / \nu_w$)) and weakly on Froude number ($Fr^2 = U_\infty^2/(g\delta_k^*)$). Schlichting's analysis includes mean profile curvature, which is an essential feature for properly characterizing the critical layer (Schlichting, 1979). By way of contrast, the analyses by Taylor (1931) and Miles & Howard (1964) neglected profile curvature, but nevertheless led to the widely quoted critical Richardson number estimate of 1/4. Although Schlichting validated his analysis using a rather limited dataset obtained in a heated channel facility at Göttingen, his work seems to have been largely ignored. We will now compare our data with his predictions.

In figure 23 we show stability curves, as calculated by Schlichting, for three Froude numbers. We see that for Reynolds numbers less than about 1000, the critical Richardson number increases very quickly for small changes in Reynolds number, but it never exceeds a value of 1/24, which is the high Reynolds number asymptote for $Fr^2 = 0$. With increasing Froude number, this value decreases, but it is only about 30% smaller for $Fr^2 = 14.65$).

We see from figure 23 that our weakly stable cases are in accord with Schlichting's theory in that they lie within the dynamically unstable region where disturbances grow (within experimental error). Also, the majority of collapsed cases fall close to the critical Richardson number curves. The collapsed cases that lie within the unstable region are also the cases with the highest wall temperatures and bulk Richardson numbers and therefore have the greatest uncertainty in wall-gradient Richardson number and friction velocity. Overall, the correspondence between Schlichting's theory and our experimental observations is encouraging for both smooth- and rough-wall cases.

7 Conclusions

The effects of stable thermal stratification on the behavior of turbulent boundary layer statistics were studied in an effort to better understand the underlying mechanisms, as well as give insight in the behavior of the atmospheric surface layer.
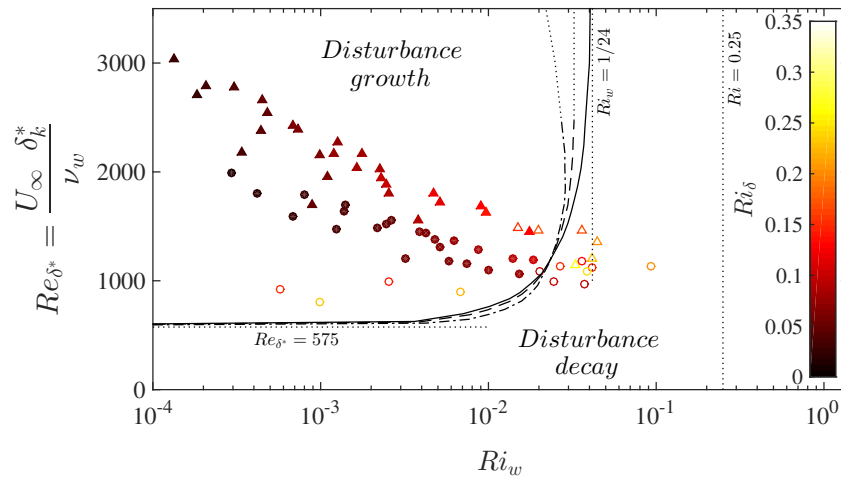
Figure 23: Conditions under which the collapse of turbulence occurs and comparisons with the linear stability theory of Schlichting (1935). All ○ smooth and △ rough wall data are included. Closed symbols represent weakly stable cases; open symbols represent collapsed cases. Lines indicate Schlichting's calculations of critical Ri_w (gradient Richardson number evaluated at the wall) as a function of $Re_{\delta_k^*}$ for ———$Fr^2 = 0$, − − −$Fr^2 = 5.86$ and $\cdot$ − $\cdot$ −$Fr^2 = 14.65$.

For weak to moderate stability levels, reductions in streamwise and wall-normal turbulence were found to be proportional to reductions in the wall shear-stress as the mean velocity profile (which obeys Zagarola-Smits outer layer scaling) progresses toward a less-full profile and the viscous layer thickens. Scaling of the turbulent stresses by the wall shear stress helps to differentiate between Reynolds and Richardson number effects, and this delineation can be further improved by the use of a density-weighted friction velocity to account for changes in fluid density in the same manner as in compressible flows. Anisotropy ratios also suggest that the characteristic angle of turbulent structures is not altered significantly for weak to moderate stability. The anisotropy ratio is not sensitive to Reynolds number and does not change significantly with increasing stratification until turbulent production by mean shear is about to collapse.

With surface roughness, the mean velocity and temperature distributions were influenced by stratification across the entire boundary layer. The small differences observed in scaled turbulence profiles between the smooth and rough-wall results are likely to be due to changes in local stratification (that is, gradient Richardson number). Overall, the rough-wall results were found to follow the smooth-wall trends with the additional benefit of covering a wider range of Reynolds numbers. This observation also implies that the smooth-wall data were not affected by transitional effects.

For weak to moderate stability levels, the turbulence structure appears little affected by stratification, even as the mean velocity and temperature profiles undergo significant changes in shape due to decreased mixing. Within this regime, all changes in turbulence intensity appear consistent with the reductions in Reynolds number imposed by stability.

For strong stability levels, there is a marked change in the flow response. Vertical transport is reduced to the point where the turbulent production by mean shear collapses, and the turbulent stresses no longer scale with the wall stress. The collapse occurs at a bulk Richardson number of $Ri_\delta = 0.1$ and $Ri_\delta = 0.15$ for the smooth and rough wall, respectively. The shape factor of the mean velocity profile in this regime is similar to that seen in a laminar Blasius boundary layer. This stronger stability or collapsed regime is characterized by weak turbulence that no longer scales with the mean wall shear stress and where the large scale motions have a more horizontal structure. Quadrant analysis indicates that only the motions that contribute to positive turbulent production were influenced by stratification. Of these, the ejections, which move away from the wall, were found to be damped to a greater degree than sweeps, which move toward the wall.

This delineation of weak and strongly stable regimes based on the scaling of the turbulent stresses is in contrast to that proposed by Ohya *et al.* (1997) and Ohya (2001), who characterized a strongly stable regime by the preferential near-wall damping of turbulence that appeared for bulk Richardson numbers above 0.25. Our results indicate instead that turbulence is preferentially damped in the outer flow, and continues to display a peak in intensity near the wall, even for the strongest stability cases where Ri_δ approaches 0.25.

The sensitivity to surface roughness of critical bulk Richardson number separating these two regimes could have implications for stable atmospheric flows over ice or salt flats compared to more typical rough earth surfaces. In addition, it seems likely that the bulk Richardson number is too crude a measure to delineate regimes over a wide range

of conditions. The current results are instead consistent (within experimental error) with collapse occurring at a critical Monin-Obukhov length based Reynolds number of close to 100, as suggested by Flores & Riley (2011) and the linear stability theory of Schlichting (1935), where the critical wall-gradient Richardson number is a function of Reynolds and Froude numbers. Schlichting's critical wall-gradient Richardson number has a maximum of 1/24 for $Fr = 0$ and reduces with Reynolds number and increasing Froude number. Both of these measures are preferred to the bulk Richardson number for the delineation of stability regimes as they involve fluxes and gradients taken at the wall.

Finally, good correspondence was observed between the current experiments and atmospheric data in the gradient Richardson number scaling of Sorbjan (2010), at least for locations outside the near-wall viscous region. This result suggests that the effects of Reynolds number on turbulent velocity statistics can be largely accounted for through known scaling techniques and that many aspects of the atmospheric surface layer can be investigated using results from relatively low-Reynolds number stably stratified laboratory experiments. Reynolds number effects however may continue to be significant for turbulence collapse at the highest stabilities as we show in section 6.1, and for other properties such as the heat transfer coefficients of rough walls Li *et al.* (2016).

8 Acknowledgements

References

ADRIAN, R. J., MEINHART, C. D. & TOMKINS, C. 2000 Vortex organization in the outer region of the turbulent boundary layer. *Journal of Fluid Mechanics* **422**, 1–54.

ARYA, S. P. S. 1968 Structure of stably stratified turbulent boudary layer. PhD thesis, Colorado State University.

ARYA, S. P. S. 1975 Buoyancy effects in a horizontal flat plate boundary layer. *Journal of Fluid Mechanics* **68**, 321–343.

ARYA, S. P. S. & PLATE, E. J. 1969 Modeling of the stably stratified atmospheric boundary layer. *Journal of Atmospheric Sciences* **26**, 656–665.

AUBERTINE, C. D. & EATON, J. K. 2005 Turbulence development in a non-equilibrium turbulent boundary layer with mild adverse pressure gradient. *Journal of Fluid Mechanics* **532**, 345–364.

BLACKADAR, A. K. 1962 The vertical distribution of wind and turbulent exchange in neutral atmosphere. *Journal of Geophysical Research* **67**, 3095–3103.

BOU-ZEID, E., HIGGINS, C., HUWALD, H., MENEVEAU, C. & PARLANGE, M. B. 2010 Field study of the dynamics and modelling of subgrid-scale turbulence in a stable atmospheric surface layer over a glacier. *Journal Of Fluid Mechanics* **665**, 480–515.

CASTILLO, L. & GEORGE, W. K. 2001 Similarity analysis for turbulent boundary layer with pressure gradient: Outer flow. *AIAA Journal* **39** (1), 41–47.

CHUNG, D. & MATHEOU, G. 2012 Direct numerical simulation of stationary homogeneous stratified sheared turbulence. *Journal of Fluid Mechanics* **696**, 434–467.

CLAUSER, F. H. 1954 Turbulent boundary layers in adverse pressure gradients. *Journal of Aeronautical Sciences* **21** (91–108).

CONNELLY, J. S., SCHULTZ, M. P. & FLACK, K. A. 2006 Velocity-defect scaling for turbulent boundary layers with a range of relative roughness. *Experiment in Fluids* **40**, 188–195.

DEMARCO, G., PUHALES, F., ACEVEDO, O. C., COSTA, F. D., AVELAR, A. C. & FISCH, G. 2015 Dependence of turbulence-related quantities on the mechanical forcing for wind tunnel stratified flow. *American Journal of Environmental Engineering* **5** (1A), 15–26.

VAN DRIEST, E. R. 1951 Turbulent boundary layer in compressible fluids. *Journal of the Aeronautical Sciences* **18**, 145–160.

VAN DRIEST, E. R. 1956 On turbulent flow near a wall. *Journal of the Aeronautical Sciences* **23**, 1007–1011 and 1036.

FLACK, K. A., SCHULTZ, M. P. & CONNELLY, J. S. 2007 Examination of a critical roughness height for outer layer similarity. *Physics of Fluids* **19**.

FLACK, K. A., SCHULTZ, M. P. & SHAPIRO, T. A. 2005 Experimental support for Townsend's Reynolds number similarity hypothesis on rough walls. *Physics of Fluids* **17**.

FLORES, O. & RILEY, J. J. 2011 Analysis of turbulence collapse in the stably stratified surface layer using direct numerical simulation. *Boundary-Layer Meteorology* **139**, 241–259.

GRACHEV, A., ANDREA, E., FAIRALL, C., GUEST, P. & PERSSON, P. 2008 Turbulent boundary layer measurements in the stable atmospheric boundary layer during SHEBA: Ten years after. *Acta Geophysica* **56** (1), 142–166.

GRACHEV, A., ANDREAS, E., FAIRALL, C., GUEST, P. & PERSSON, P. 2007 SHEBA flux-profile relationships in the stable atmospheric boundary layer. *Boundary-Layer Meteorology* **124**, 315–333.

GRACHEV, A., ANDREAS, E., FAIRALL, C., GUEST, P. & PERSSON, P. 2015 Similarity theory based on the Dougherty–Ozmidov length scale. *Quarterly Journal Royal Meteorological Society* **141**, 1845–1856.

GRACHEV, A., FAIRALL, C., PERSSON, P., ANDREAS, E. & GUEST, P. 2005 Stable boundary layer scaling regimes: the SHEBA data. *Boundary-Layer Meteorology* **116**, 201–235.

HAMA, F. R. 1954 Boundary-layer characteristics for rough and smooth surfaces. *SNAME* .

HUANG, H. T., FIEDLER, H. E. & WANG, J. J 1993 Limitation and improvement of PIV. II - Particle image distortion, a novel technique. *Experiment in Fluids* **15**, 168–174.

HUANG, J. & BOU-ZEID, E. 2013 Turbulence and Vertical Fluxes in the Stable Atmospheric Boundary Layer. Part I: A Large-Eddy Simulation Study. *Journal Of The Atmospheric Sciences* **70**, 1513–1527.

JAMBUNATHAN, K., JU, X. Y., DOBBINS, B. N. & ASHFORTH-FROST, S. 1995 An improved cross-correlation technique for particle image velocimetry. *Measurement Science and Technology* **6** (5), 507.

JIMENEZ, J. 2004 Turbulent flows over rough walls. *Annual Review in Fluid Mechanics* **36**, 173–196.

KAIMAL, J. C., WYNGAARD, J., IZUMI, Y. & COTÉ, O. R. 1972 Spectral characteristics of surface layer turbulence. *Quarterly Journal of the Royal Meteorological Society* **98**, 563–589.

KATUL, G. G., PORPORATO, A., SHAH, S. & BOU-ZEID, E. 2014 Two phenomenological constants explain similarity laws in stably stratified turbulence. *Physical Review E* **89** (2).

LI, Q, BOU-ZEID, E., ANDERSON, W., GRIMMOND, S. & HULTMARK, M. 2016 Quality and reliability of les of convective scalar transfer at high reynolds numbers. *International Journal of Heat and Mass Transfer* **102** (959–970).

LIGRANI, P. M. & MOFFAT, R. J. 1986 Structure of transitional rough and fully rough turbulent boundary layers. *Journal of Fluid Mechanics* **162**, 69–98.

LU, S. S. & WILLMARTH, W. W. 1973 Measurements of the structure of the Reynolds stress in a turbulent boundary layer. *Journal of Fluid Mechanics* **60**, 481.

MAHRT, L. 1998 Stratified atmospheric boundary layers and breakdown of models. *Theoretical and Computational Fluid Dynamics* **11**, 263–279.

MAHRT, L. 2014 Stably stratified atmospheric boundary layers. *Ann. Rev. Fluid Mech.* **46**, 23–45.

McKeon, B. J., Li, J. D., Jiang, W., Morrison, J. F. & Smits, A. J. 2004 Further observations on the mean velocity distribution in fully developed pipe flow. *Journal of Fluid Mechanics* **501**, 135–147.

Miles, J. W. & Howard, L. N. 1964 Note on heterogenous shear flow. *Journal of Fluid Mechanics* **20** (2), 331–336.

Monin, A. S. & Obukhov, A. M. 1954 Basic laws of turbulent mixing in the surface layer of the atmosphere. *Contrib. Geophys. Inst. Acad. Sci. USSR* **151**, 163–187.

Morkovin, M. V. 1961 Effects of compressibility on turbulent flows. In *International Symposium on the mechanics of turbulence, Paris.*

Nicholl, C. I. H. 1970 Some dynamical effects of heat on a turbulent boundary layer. *Journal of Fluid Mechanics* **40** (2), 361–384.

Nieuwstadt, F. T. M. 1984 The turbulent structure of the stable, nocturnal boundary layer. *Journal of Atmospheric Sciences* **41**, 2202–2216.

Nieuwstadt, F. T. M. 1985 A model for the stationary, stable boundary layer. In *Turbulence and diffusion in stable environments* (ed. J. C. R. Hunt), pp. 149–179. Oxford: Oxford [Oxfordshire] : Clarendon Press ; New York : Oxford University Press.

Nikuradse, J. 1933 Laws of flow in rough pipes. *Tech. Rep.* NACA TM 1292.

Nogueira, J., Lecuona, A. & Rodriguez, P. A. 1999 Local field correction PIV: on the increase of accuracy of digital PIV systems. *Experiment in Fluids* **27** (2), 107–116.

Ogawa, Y., Diosey, K., Uehara, K. & Ueda, H. 1985 Wind tunnel observation of flow and diffusion under stable stratification. *Atmospheric Environment* **19**, 65–74.

Ogawa, Y., Diosey, P. G., Uehara, K. & Ueda, H. 1982 Plume behavior in stratified flows. *Atmospheric Environment* **16** (6), 1419–1433.

Ohya, Y. 2001 Wind-tunnel study of atmospheric stable boundary layers over a rough surface. *Boundary-Layer Meteorology* **98**, 57–82.

Ohya, Y., Neff, D. E. & Meroney, R. N. 1997 Turbulence structure in a stratified boundary layer under stable conditions. *Boundary-Layer Meteorology* **83**, 139–161.

Ohya, Y. & Uchida, T. 2003 Turbulence structure of stable boundary layers with a near-linear temperature profile. *Boundary-Layer Meteorology* **108**, 19–38.

Ohya, Y. & Uchida, T. 2004 Laboratory and numerical studies of the convective boundary layer capped by a strong inversion. *Boundary-Layer Meteorology* **112**, 223–240.

Panton, R. L. 1990 Scaling turbulent wall layers. *Journal of Fluids Engineering* **112** (4), 425–432.

Perry, A. E., Schofield, W. H. & Joubert, P. N. 1969 Rough wall turbulent boundary layers. *Journal of Fluid Mechanics* **37** (2), 383–413.

PIAT, J.-F. & HOPFINGER, E. J. 1981 A boundary layer topped by a density interface. *Journal of Fluid Mechanics* **113**, 411–432.

PLATE, E. J. & ARYA, S. P. S. 1969 Turbulence spectra in a stably stratified boundary layer. *Radio Science* **4** (12), 1163–1168.

PRASAD, A. K., ADRIAN, R. J., LANDRETH, C. C. & OFFUTT, P. W. 1992 Effect of resolution on the speed and accuracy of Particle Image Velocimetry interrogation. *Experiment in Fluids* **13** (2–3), 105–116.

PUHALES, F. S., DEMARCO, G., MARTINS, L. G. N., ACEVEDO, O. C., DEGRAZIA, G. A., WELTER, G. S., COSTA, F. D., FISCH, G. F. & AVELAR, A. C. 2015 Estimates of turbulent kinetic energy dissipation rate for a stratified flow in a wind tunnel. *Physica A* **431**, 175–187.

SCARANO, F. 2002 Iterative image deformation methods in PIV. *Measurement Science and Technology* **13** (1).

SCHLICHTING, H. 1935 Hauptaufsätze. Turbulenz bei wärmeschichtung. *ZAMM-Journal of Applied Mathematics and Mechanics/Zeitschrift für Angewandte Mathematik und Mechanik* **15** (6), 313–338, [Translation by Cedrick Ansorge, 2014 - https://www.researchgate.net/publication/264508137_Turbulence_ under_Stratification_H_Schlichting].

SCHLICHTING, H. 1979 *Boundary-layer Theoryt*. McGraw-Hill.

SCHUMANN, U. & GERZ, T. 1995 Turbulent mixing in stably stratified shear flows. *Journal of Applied Meteorology* **34** (1), 33–48.

SHAH, S. K. & BOU-ZEID, E. 2014 Direct numerical simulations of turbulent Ekman layers with increasing static stability: modifications to the bulk structure and second-order statistics. *Journal of Fluid Mechanics* **760**, 494–539.

SMITS, A. J. & DUSSAGE, J.-P. 2005 *Turbulent Shear Layers In Supersonic Flow*, 2nd edn. Springer-Verlag New York Inc.

SMITS, A. J., MATHESON, N. & JOUBERT, P. N. 1983 Low reynolds number turbulent boundary layers in zero and favourable pressure gradients. *Journal of Ship Research* **27**, 147–157.

SORBJAN, Z. 2010 Gradient-based scales and similarity laws in the stable boundary layer. *Quarterly Journal of the Royal Meteorological Society* **136**, 1243–1254.

SORBJAN, Z. 2012 The height correction of similarity functions in the stable boundary layer. *Boundary-Layer Meteorology* **142**, 12–31.

STULL, R. B. 1988 *An introduction to boundary layer meteorology*, , vol. 13. Springer.

TAYLOR, G. I. 1931 Effect of variation in density on the stability of superimposed streams of fluid. *Proceedings of the Royal Society A* **132**, 499.

Townsend, A. A. 1976 *The structure of turbulent shear flows*. Cambridge University press.

Westerweel, J. & Scarano, F. 2005 Universal outlier detection for PIV data. *Experiments in Fluids* **39** (6), 1096–1100.

Williams, O. J. H. 2014 Density effects on turbulent boundary layer structure: from the atmosphere to hypersonic flow. PhD thesis, Princeton University.

Wu, Y. & Christensen, K. T. 2006 Population trends of spanwise vortices in wall turbulence. *Journal of Fluid Mechanics* **568** (55-76).

Zagarola, M. V. & Smits, A. J. 1998*a* Mean-flow scaling of turbulent pipe flow. *Journal of Fluid Mechanics* **373**, 33–79.

Zagarola, M. V. & Smits, A. J. 1998*b* A new mean velocity scaling for turbulent boundary layers. In *ASME Paper No. FEDSM98-4950*.

Zilitinkevich, S. S., Elperin, T., Kleeorin, N., Rogachevskii, I. & Esau, I. 2013 A hierarchy of energy- and flux-budget (EFB) turbulence closure models for stably-stratified geophysical flows. *Boundary-Layer Meteorology* **146**, 341–373.